HHS Public Access

Author manuscript

Cell. Author manuscript; available in PMC 2022 June 14.

Published in final edited form as:

Cell. 2021 April 01; 184(7): 1790–1803.e17. doi:10.1016/j.cell.2021.02.015.

B cell-specific XIST complex enforces X-inactivation and restrains atypical B cells

Bingfei Yu[1], **Yanyan Qi**[1], **Rui Li**[1], **Quanming Shi**[1], **Ansuman T. Satpathy**[3], **Howard Y. Chang**[1,2,4]

[1]Center for Personal Dynamic Regulomes, Stanford University, Stanford, CA, 94305, USA.

[2]Howard Hughes Medical Institute, Stanford University, Stanford, CA, 94305, USA.

[3]Department of Pathology, Stanford University, Stanford, CA, 94305, USA.

[4]Lead Contact

SUMMARY

The long non-coding RNA (lncRNA) XIST establishes X chromosome inactivation (XCI) in female cells in early development and thereafter is thought to be largely dispensable. Here we show XIST is continually required in adult human B cells to silence a subset of X-linked immune genes such as *TLR7*. XIST-dependent genes lack promoter DNA methylation and require continual XIST-dependent histone deacetylation. XIST RNA-directed proteomics and CRISPRi screen reveal distinctive somatic cell-type-specific XIST complexes, and identify TRIM28 that mediates Pol II pausing at promoters of X-linked genes in B cells. Single-cell transcriptome data of female patients with either systemic lupus erythematosus or COVID-19 infection revealed XIST dysregulation, reflected by escape of XIST-dependent genes, in CD11c+ atypical memory B cells (ABCs). XIST inactivation with TLR7 agonism suffices to promote isotype-switched ABCs. These results indicate cell-type-specific diversification and function for lncRNA-protein complexes and suggest expanded roles for XIST in sex-differences in biology and medicine.

In Brief

XIST restrains human atypical B cell development. A distinct XIST-associated protein complex contributes to XIST-mediated gene silencing in B cells.

Graphical Abstract

Correspondence to: howchang@stanford.edu.

AUTHOR CONTRIBUTIONS

B.Y. and H.Y.C conceived the project. B.Y. performed most experiments and analyzed the data. Y.Q. and A.T.S. performed CHIRP-MS. R.L. performed RNA-seq library preparation. Q.S. performed TRIM28 mutants cloning. B.Y. and H.Y.C. wrote the manuscript with input from all authors. H.Y.C. supervised the work and acquired the funding.

DECLARATION OF INTERESTS

H.Y.C. is a co-founder of Accent Therapeutics, Boundless Bio, and an advisor to 10x Genomics, Arsenal Biosciences, and Spring Discovery. A.T.S. is a founder of Immunai and Cartography Biosciences and receives research funding from Arsenal Biosciences and 10x Genomics.

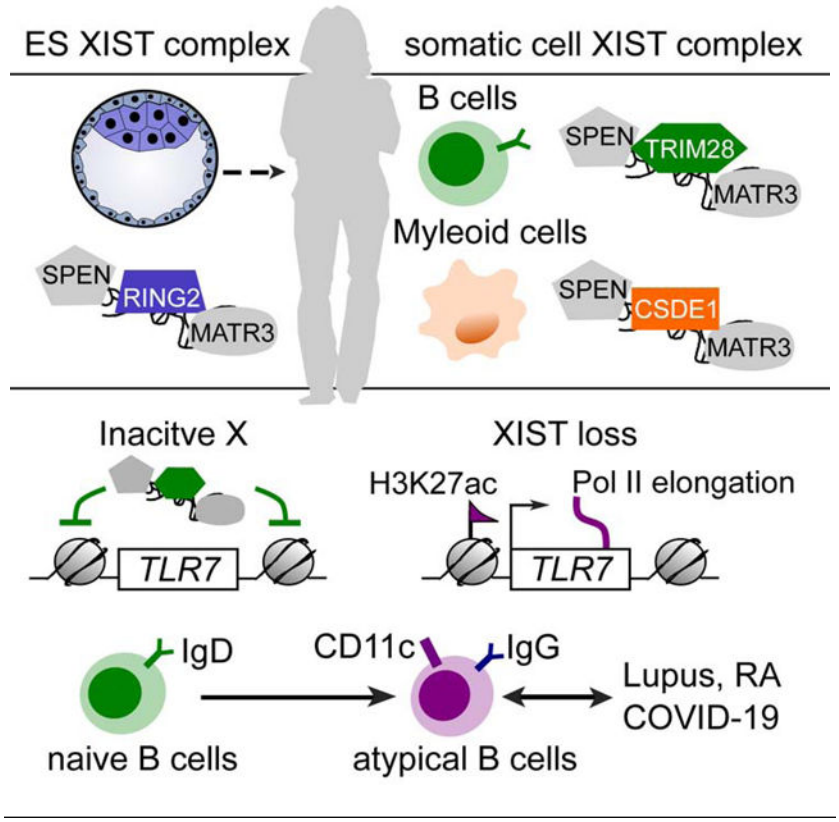

INTRODUCTION

Eutherian mammals have evolved a unique strategy to epigenetically silence one of the two X chromosomes (chrX) in females, a process termed X chromosome inactivation (XCI) (Lyon, 1962). XCI is comprised of initiation, establishment and maintenance. During early embryogenesis, XCI is initiated by XIST, a lncRNA that is transcribed and spreads in *cis* across the entire inactive X (Xi) (Penny et al., 1996). Once XCI is established, the Xi is stably silenced via epigenetic mechanisms such as DNA methylation (Gartler and Riggs, 1983). Nonetheless, over 20% of X-linked genes (termed escapees) escape from XCI (Carrel and Brown, 2017). Some escapees are tissue-specific, highlighting a diversity of XCI maintenance across different tissues (Oliva et al., 2020; Tukiainen et al., 2017). Despite its central role in XCI initiation and establishment, XIST was long thought to be dispensable for XCI maintenance. Genetic deletion of XIST in cultured somatic cells did not reactivate the Xi (Brown and Willard, 1994; Csankovszki et al., 1999). However, recent studies with conditional knockout of mouse *Xist* in different tissues led to partial Xi reactivation (Adrianse et al., 2018; Yang et al., 2016, 2020). These observations highlight the need to understand when and where XIST is needed for XCI maintenance.

XIST lncRNA comprises several functional modules including A-F repeats (Lu et al., 2017). These repeats can bind and recruit diverse proteins that are responsible for chromatin modification, transcriptional silencing, XIST RNA spreading and coating (Chu et al., 2015; Loda and Heard, 2019). At the onset of XCI, XIST recruits SPEN via A-repeat to facilitate histone deacetylation (Dossin et al., 2020; Lu et al., 2016; Żylicz et al., 2019). Then XIST

B and C repeat binding protein HNRNPK recruits Polycomb repressive complex (PRC) 1 and 2, which are responsible for later accumulation of repressive marks H2AK119b and H3K27me3 respectively, further locking in silencing (Almeida et al., 2020). XIST tethering to the Xi relies on C repeat binding protein HNRNPU and E repeat binding protein CIZ1 (Hasegawa et al., 2010; Sunwoo et al., 2017). Although XIST co-factors are well characterized during XCI initiation, the nature and function of the XIST ribonucleoprotein (RNP) complex during XCI maintenance in adult somatic cells is virtually unknown.

Escape from XCI has long been thought to contribute to sex differences. Because chrX harbors a high density of immune genes, incomplete XCI maintenance may lead to elevated X-linked immune gene dosage in females over males, contributing to female-biased autoimmune diseases (Klein and Flanagan, 2016). Indeed, 80% of patients with autoimmune diseases are women and such female-bias can be linked to the dosage of X-linked immune genes (Libert et al., 2010). For example, *TLR7,* an X-linked gene encoding Toll-like receptor 7, recognizes single-strand (ss) RNA-containing immune complexes that involve in female-biased autoimmunity and ssRNA viral infection (Celhar et al., 2012). The duplication of *Tlr7* gene in mice suffices to drive lupus-like symptoms whereas the deletion of *Tlr7* ameliorates the disease (Christensen et al., 2006; Subramanian et al., 2006). An important consequence of elevated TLR7 signaling is the formation and activation of CD11c+ atypical memory B cells (ABCs) (Hao et al., 2011; Rubtsov et al., 2011; Rubtsova et al., 2015). ABCs are a unique B cell population that greatly expands in aging, certain infectious diseases (malaria, HIV, and COVID-19 (Woodruff et al., 2020)), and female-biased autoimmunity (systemic lupus erythematosus (SLE) and rheumatoid arthritis (RA)) (Cancro, 2020; Karnell et al., 2017). ABCs accumulate in aged female mice but not in age-matched male mice (Rubtsov et al., 2011). A recent study showed a complete lack of XIST localization on the Xi in CD11c+ ABCs (Pyfrom et al., 2020). Such abnormal XIST localization has also been observed in patients with SLE where CD11c+ atypical B cells are expanded (Wang et al., 2016) (Wang et al., 2016). How and why ABCs are female-biased and potential links to XIST action are largely unknown.

Here, we investigate the role of XIST for XCI maintenance in human B cells. We identify X-linked genes that require ongoing XIST-mediated silencing, characterize the required epigenomic mechanisms, and uncover XIST dysregulation in atypical B cells in multiple human disease states.

RESULTS

XIST is essential for maintaining X-inactivation of immune genes in human B cells

To determine if the XCI is maintained by XIST-mediated silencing or epigenetic memory such as DNA methylation and H3K27me3, we performed CRISPR interference (CRISPRi) of XIST in GM12878 B cells (sgXIST group), a female human B cell line with normal karyotype, leading to 75% XIST knockdown (Figure 1A-B, Figure S1A). We also treated the cells with DNMT and EZH2 inhibitors to block DNA methylation and H3K27me3 (inhibitors group). We performed allelic RNA-seq analysis using heterozygous single nucleotide polymorphisms (SNPs) provided by the phased genome (ENCODE Project Consortium, 2012). For genes with at least 10 reads that can be assigned to alleles,

we calculate d-score to measure the allelic bias, which is defined as (reads^{Xi}/(reads^{Xi}+ reads^{Xa})-0.5). The dscore has a range of −0.5 to +0.5: −0.5 means all the reads are from the active chrX (Xa) and +0.5 means all the reads are from the inactive chrX (Xi); 0 means the reads are biallelic.

Treatment of epigenetic inhibitors led to 8066 differentially expressed genes (DEG) compared to the control group. In contrast, silencing of XIST led to only 510 DEGs (Figure S1B, Table S1). We noticed that upregulated DEGs after XIST knockdown are more enriched on chrX (24.4%) compared to inhibitors-treated cells (6.8%) (Figure S1D). These results indicated that XIST is the major contributor to maintain the gene dosage on the chrX in somatic B cells, supported by the correlation analysis of the chrX allelic bias across samples (Figure S1C). The cumulative distribution of d-scores across the chrX was significantly increased in sgXIST over control cells (p=0.002, K-S test), without changes of allelic bias on autosomes (Figure 1D-E, Figure S1E). 36 of 130 (27.6%) genes with lower expression in Xi (d-score<0) showed significantly increased d-score in sgXIST cells over control cells (d-score^{sgXIST}- d-score^{Ctrl} >0.03, binomial p<0.05), suggesting that they rely on XIST to maintain X-inactivation (Figure 1F). Thus, contrary to expectation, XIST is not fully dispensable for XCI maintenance in adult B cells.

We named these 36 genes as XIST-dependent genes, whereas the remaining 94 genes were named XIST-independent genes because their d-score is not significantly altered after XIST perturbation (Table S2). In control cells, the d-score is significantly higher in XIST-dependent compared to -independent genes, suggesting that formers are not stably silenced (Figure S1F). Indeed, we compared the proportion of variable and constitutive escapees that are defined from Genotype-Tissue Expression (GTEx) study (Tukiainen et al., 2017) and found these escapees are enriched in XIST-dependent compared to -independent genes (Figure S1G). Gene Ontology (GO) analysis of the genes upregulated in sgXIST group showed enrichment in immune response genes including *TLR7, GPR174, CXCR3, and CXCL10* (GO enrichment $p=7 \times 10^{-5}$) (Figure S1H). Immune-associated genes are more enriched in XIST-dependent genes compared to -independent genes (p=0.01, Fisher's exact test) (Figure 1G). We found increased d-score of X-linked immune genes in sgXIST group over control group, supporting that XIST is essential for Xi silencing of these genes (Figure 1H). Specifically, we observed an increased biallelic expression of *TLR7* and ~1.8 fold increase in *TLR7* bulk RNA expression after XIST knockdown (Figure 1I-J). Re-expression of XIST by introduction of anti-CRISPR protein in XIST CRISPRi B cells resilenced the Xi (Figure S1I-K), indicating XIST can re-silence a previously active X in B cells.

Analysis of XIST inactivation in human fibroblasts, mouse brain tissue, and GTEx database suggest dependence on XIST and XCI escape occur in multiple lineages with variable magnitude and tissue specificity (Figure S2A-D).

Absence of DNA methylation predicts requirement of XIST for XCI maintenance

We hypothesized that XIST-dependent genes harbor chromatin and/or genetic features that could explain their unstable silencing and continuous dependence on XIST. Indeed, we found significantly lower DNA methylation near their TSSs, and lower H3K27me3 at their gene bodies, compared to XIST-independent genes (Figure 2A-B). Promoters of XIST-

dependent genes contain fewer CpG islands (Figure S2E). DNA GC content, proximity to *XIST* locus, density of LINE, SINE, or LTR element were similar between XIST-dependent and -independent genes (Figure S2E-F). Regression analysis with all epigenomic features showed that low DNA methylation is significantly associated with the XIST-dependent genes and predicted whether the XCI maintenance of genes relies on XIST (Figure 2C-D). We then test if XIST-independent genes may become dependent on XIST for XCI maintenance when epigenetic memory is blocked. Treatment of XIST-depleted cells with epigenetic inhibitors significantly increased the d-score of XIST-independent genes compared to either perturbation alone (Figure 2E). Together, we show that XIST-dependent genes are not stably silenced due to the absence of DNA methylation. Moreover, XIST is functionally redundant with DNA methylation for the maintenance of silencing for a larger set of Xi genes.

XCI maintenance in adult B cells relies on XIST-mediated histone deacetylation

XIST is critical for XCI initiation via the deacetylation of active mark H3K27ac and the accumulation of repressive mark H3K27me3. We generated *XIST* A-repeat KO B cells by CRISPR-Cas9 as a *XIST* KO model. The genomic deletion of *XIST* A repeat (overlapped with XIST promoter) leads to >99% loss of XIST RNA, consistent with *Xist* A-repeat KO mouse study (Hoki et al., 2009) (Figure S3A-C). Epigenomic mapping showed a significant increase of H3K27ac deposition at Xi when XIST is ablated, while autosomes showed no change (Figure 3B, Figure S3D), For example, *XIST* KO led to increased H3K27ac deposition at Xi of the immune gene *GPR174* which was reported to impart sex differences in B cell migration (Zhao et al., 2020) (Figure 3A). This re-acetylation of H3K27 after the loss of XIST is preferentially enriched at XIST-dependent genes, and significantly enriched at distal enhancers rather than promoters (Figure 3B-C). This is consistent with the discovery that during XCI initiation, XIST promotes enhancer deacetylation by increasing the activity of histone deacetylase HDAC3, which pre-bound to those enhancers before XIST binding (Żylicz et al., 2019). In contrast, XIST KO did not cause significant change of H3K27me3 occupancy across Xi or at XIST-dependent genes (Figure 3D, Figure S3E). Thus, XIST is continuously required to maintain the silencing status of the Xi especially for XIST-dependent genes in part through H3K27ac deacetylation at enhancers in B cells.

XIST ChIRP-MS uncovers distinct somatic cell XIST RNP complexes for XCI maintenance

XIST is a modular lncRNA that can binds to diverse protein partners during XCI establishment (Chu et al., 2015; McHugh et al., 2015; Minajigi et al., 2015), but the composition of the XIST RNP in somatic cells is not known. We performed XIST ChIRP-MS in the B cell line GM12878 and myeloid cell line K562, which both represent somatic immune cell types with established XCI (Figure 4A, Table S3). We used formaldehyde crosslinking to detect both direct RNA-protein interactions and indirect protein-protein interactions in the XIST complex. RNAse-treated samples served as a negative control to cull non-specific proteins that bind to probes or beads (Figure S4A-B).

Two replicates of XIST ChIRP-MS data in B cells identified 115 XIST binding proteins (Figure S4C). These XIST co-factors can be segregated into groups based on their functions, including chromatin enzymes, nuclear matrix, m6A methylation, and RNA splicing (Figure

4B). The transcriptional repressor SPEN is recruited to Xi by XIST A-repeat and promotes gene silencing via modulating HDAC activity (Dossin et al., 2020; McHugh et al., 2015). We further found distinct XIST binding proteins in B cells such as TRIM28 (also known as KAP1), an epigenetic co-repressor that can bridge multiple histone modifiers for repression (Czerwińska et al., 2017; Iyengar and Farnham, 2011). To determine if the XIST RNP complex is similar between XCI establishment and maintenance, we compared the enrichment of peptide counts for XIST co-factors between B cells and ES cells with inducible expression of XIST. We found 57.8% of XIST co-factors are shared between initiation and maintenance (Figure 4C). This comparison revealed maintenance-specific XIST RNP subunits including RNF40 and TRIM28, suggesting XIST may recruit specific proteins for XCI maintenance. We further compared XIST co-factors between B cells and myeloid cells and found that 71.3% of XIST binding proteins are shared, suggesting that XIST-RNP also has cell-type specific subunits in somatic cells. Notably, TRIM28 is a B cell-specific XIST cofactor, suggesting that TRIM28 might be essential for XIST-mediated XCI maintenance in B cells (Figure 4D). TRIM28 fRIP-qRT-PCR specifically retrieved XIST RNA only in B cells but not in K562 myeloid cells or differentiating ESCs (Figure S4D), further validating that TRIM28 is a B cell-specific XIST binding protein. The XIST interactome in somatic immune cells identified a catalog of cell-type-specific XIST co-factors.

Allelic CRISPRi screen reveals essential XIST co-factors for XCI maintenance in B cells

To functionally validate if the XIST co-facotrs revealed by ChIRP-MS are essential for XCI maintenance, we developed a CRISPRi screen in the dCas9-KRAB expressed B cell line. The readout is the allelic expression of *TLR7*, an X-linked immune gene whose biallelic expression is associated with female-biased autoimmunity (Souyris et al., 2018). We selected 57 high-confidence XIST co-factors in B cells with a stringent cutoff (peptide counts>25, fold enrichment>10). We designed two sgRNAs targeting TSS adjacent regions per gene and cloned two sgRNAs under human or mouse U6 promoters in the same lentiviral vector. After individual sgRNA transduction and puromycin selection, we enriched for cells undergoing CRISPRi and isolated RNA for *TLR7* allelic library preparation (Figure 5A, Table S4).

Depletion of 7 out of 57 XIST cofactors individually increased the d-score of *TLR7* compared to non-targeting sgRNA control, suggesting that these co-factors are critical for XCI maintenance of *TLR7* (cut-off delta d-score: $\text{d-score}^{\text{co-factor}} - \text{d-score}^{\text{Ctrl}} > 0.1$) (Figure 5B). The 7 key XIST co-factors are SPEN, TRIM28, RNF20, RNF40, PTBP1, MATR3, and HNRNPA0, and the first 4 proteins are involved in chromatin modification (Figure 5C). Notably, despite similar XIST binding affinity and perturbation efficiency as XIST A-repeat binding factor SPEN, depletion of XIST repeat B or C binding factors HNRNPK and HNRNPU did not affect XCI maintenance (Figure 5D, Figure S5A). The results indicated that HNRNPK-recruited PRC complexes and subsequent H3K27me3 deposition may be dispensable for XCI maintenance, highlighting SPEN-mediated H3K27ac deacetylation for XCI maintenance (Figure 3E; Figure 5D). To test this, we generated a SPEN mutant B cell line with deletion of SPEN RRM2-4 domain, which directly interacts with XIST for gene silencing (Carter et al., 2020; Dossin et al., 2020; Monfort et al., 2015) (Figure S5B).

SPEN mutation led to significant reactivation of Xi specifically at XIST-dependent genes (Figure S5C-D). These data fully support that XIST recruits SPEN to maintain XCI likely via SPEN-HDAC3 mediated H3K27 deacetylation.

PTBP1 and MATR3 have been recently reported to regulate XCI maintenance (Pandya-Jones et al., 2020). PTBP1 and MATR3 are not required for establishment of XCI but only for maintenance in ES cells, which is consistent with our discovery of both factors as required to maintain XCI in adult B cells. Importantly, depletion of B cell-specific XIST cofactor TRIM28 led to Xi reactivation of *TLR7*, indicating that potential TRIM28-mediated mechanisms participate in XCI maintenance (Figure 5C).

TRIM28 is required for B cell XCI maintenance of a subset of X-linked genes

To further determine if TRIM28 is critical for XCI maintenance, we generated *TRIM28* KO B cells, which reduced TRIM28 protein by >95% (Figure S6A). *TLR7* was indeed reactivated on Xi in *TRIM28*-KO cells (Figure 6A). However, d-score analysis across chrX showed a modest effect on Xi reactivation in *TRIM28* KO cells (Figure 6B). TRIM28 loss leads to increased d-score in only a subset of genes and 64.7% of them are also XIST-dependent (Figure 6C). The increased d-score of the TRIM28-dependent genes ($d\text{-score}^{\text{TRIM28 KO}}$-$d\text{-score}^{\text{Ctrl}}$ >0.03) is due to re-activation of Xi without significant change on Xa (Figure S6B). ChIP-seq analysis showed TRIM28 occupied *ZNF* genes on autosomes with concordant deposition of the repressive mark H3K9me3 (Figure S6C), as expected (Iyengar and Farnham, 2011). On chrX, TRIM28 is enriched at the promoters of TRIM28-dependent genes, such as *TXLNG* compared to TRIM28-independent genes (Figure 6D-E). Allelic analysis of TRIM28 ChIP-seq data revealed that TRIM28 binds to both Xa and Xi (Figure S6D). We compared the allele bias of TRIM28 binding between TRIM28-dependent and independent genes, and found a significantly increased binding at Xi rather than Xa of TRIM28-dependent genes compared to -independent genes (p=0.0008, Wilcoxon rank-sum test) (Figure S6E).

TRIM28 is a transcriptional co-repressor that can evoke several silencing mechanisms. These include recruitment of SETDB1, a histone methyltransferase for H3K9me3, interaction with HDAC-NuRD complex for histone deacetylation, or inhibition of pTEFb to impact RNA polymerase (Pol II) pause release (Ma et al., 2019; Schultz et al., 2001, 2002). Therefore, we examined diagnostic epigenomic features of each of these mechanisms in turn. We observed variable H3K9me3 deposition between TRIM28-dependent and -independent X-linked immune genes (Figure S6F). We also observed a higher H3K27ac at promoters of TRIM28-dependent genes and no significant difference of H3K9me3 and H3K27me3 (Figure S6G), suggesting an alternative regulatory mechanism of TRIM28 beyond erasing H3K27ac or writing H3K9me3. We compared the binding profile of RNA Pol II, Pol II Ser5 phosphorylation (Ser5P, transcription initiation mark), and Pol II Ser2 phosphorylation (Ser2P, transcription elongation mark) between TRIM28-dependent and -independent genes. We found Ser2P enrichment at the promoter relative to the gene body is significantly higher in TRIM28-dependent over -independent genes, whereas their Ser5P occupancy levels are quite similar (Figure 6F). This result indicates that TRIM28-dependent

genes may possess higher promoter-proximal pausing of Ser2P Pol II and thus less efficient transcription elongation.

We further measured the Pol II promoter-proximal pausing ratio using GRO-seq data (Core et al., 2014). Indeed, there is a dramatic enrichment of nascent RNA at the promoter of TRIM28-dependent gene *TLR7*, but not for TRIM28-independent gene *SASH3* (Figure S6H). We found a significantly higher promoter-proximal pausing for TRIM28-dependent genes, suggesting that TRIM28 occupancy may inhibit transcription elongation of these genes to maintain XCI (Figure 6G). The RING domain of TRIM28 is responsible for CDK9 sumoylation to inhibit CDK9 kinase activity, that is essential for transcription elongation (Ma et al., 2019) (Ma et al., 2019). The PHD domain of TRIM28 sumoylates adjacent Bromodomain (BR) domain, facilitating recruitment of SETDB1 (Czerwińska et al., 2017). We re-introduced TRIM28 full length protein or TRIM28 mutants with RING domain or PHD-BR (PB) domain deletion into TRIM28 KO cells (Figure S6I). We also created SETDB1 CRISPRi cells which led to 82% knockdown of SETDB1 (Figure S6J). Allelic analysis by pyrosequencing on three TRIM28-dependent immune genes showed that full length TRIM28 protein rescued the TRIM28 KO for gene silencing as expected. Deletion of TRIM28 RING domain led to significant reactivation of all three TRIM28-dependent genes, suggesting RING domain-mediated CDK9 sumoylation and Pol II pausing are important for XCI maintenance of these genes. In contrast, deletion of TRIM28 PB domain or SETDB1 depletion had little effect on the allelic bias, indicating PB domain mediated SETDB1 recruitment and SETDB1-mediated H3K9me3 are dispensable (Figure S6K).

Next, we performed TRIM28 RIP-qRT-PCR to assess the domain of XIST RNA that interacts with TRIM28 (Figure 6H). TRIM28 immunoprecipitation with formaldehyde crosslinking, but not UV crosslinking, specifically retrieved endogenous XIST A-repeat but not other portions, suggesting that TRIM28 indirectly interacts with XIST possibly through interaction of XIST A-repeat binding proteins (Figure 6H-I).

Finally, to test if TRIM28 is required in XCI maintenance in a B cell-specific manner, we analyzed the published shRNA screen data in differentiated ES cells with inducible XIST expression and a GFP reporter (Moindrot et al., 2015). We found that TRIM28 shRNA is not enriched in GFP^{hi} cells (Figure S6L), suggesting that TRIM28 is not required for X-inactivation in differentiated ES cells. We also performed TRIM28 CRISPRi in K562 myeloid cells and achieved ~70% knockdown of TRIM28 (Figure S6M). The loss of TRIM28 lead to a significant upregulation of four TRIM28-dependent X-linked genes only in B cells but not in myeloid cells (Figure S6N). ChIP-seq analysis showed TRIM28 occupied these gene loci only in B cells (Figure S6N). Thus, both functional and biochemical evidence indicate cell-type specific action of TRIM28 on Xi genes in B cells.

Taken together, these results suggest that B cell-specific XIST cofactor TRIM28 may prevent efficient transcription elongation via RING domain-mediated sumoylation to maintain X-inactivation in B cells (Figure 6I).

Escape of XIST-dependent genes in CD11c+ atypical B cells

Increased expression of X-linked genes along with the aberrant XIST localization was observed in immune cells from SLE patients, suggesting abnormal XCI maintenance may predispose women to autoimmune diseases (Syrett et al., 2019). We performed functional annotation analysis on genes that are overexpressed after XIST depletion in human B cell line. The result showed significant enrichment of genes related to IFN-γ cytokine production, and female-biased autoimmune diseases SLE and RA (Figure 7A), suggesting that XIST-mediated XCI maintenance may be essential to prevent overexpression of X-linked genes that may contribute to autoimmunity. To test this, we used gene set enrichment analysis (GSEA) and found that genes normally silenced by XIST tend to be over-expressed in patients with SLE compared to healthy donors (Figure S7A). Recent studies showed that IgD-CD27-CD11c+ atypical B cells (ABCs) are induced by TLR7 and contribute to pathogenic responses in SLE (Jenks et al., 2018). Our GSEA result showed that XIST-silenced genes tend to be over-expressed in these ABCs of SLE patients (Figure S7A). To further explore the impact of XIST-mediated XCI maintenance in SLE, we leveraged our discovery of “XIST-dependent” genes (X-linked genes whose maintenance are dependent on XIST) and “XIST-independent” genes (control X-linked genes whose maintenance are not). The GSEA analysis showed that XIST-dependent genes are significantly overexpressed in PBMC and IgD-CD27-CD11c+ ABCs of female SLE patients, while the XIST-independent genes were not (Figure 7B, Figure S7B). These results highlight the potential role of XIST dysregulation and subsequent escape of XIST-dependent genes in specific B cell subsets (CD11c+ ABCs) in certain diseases.

We developed a single cell gene expression score, termed “XIST escape score”, to evaluate XIST dysregulation in single cell transcriptome data across diverse human disease states. The XIST escape score is the normalized mean expression value of the XIST-dependent X-linked gene set minus that of the XIST-independent gene set. Thus, the score reflects the coordinate induction of XIST-dependent genes while controlling for overall X-linked gene expression. Applying the XIST escape score to 11 human immune cell scRNA-seq data sets, we discovered specific disease states and B cell subsets where XIST dysregulation occur in vivo (Table S7). Interestingly, we found that escape of XIST-dependent genes occurs during COVID-19 infection, specifically in CD11c+ ABCs (Figure 7C-D). Single cell analysis distinguished CD11c+ ABCs from naive B and conventional memory cells (Figure S7C-D). Cell fate trajectory analysis revealed a bifurcation of the differentiation trajectory from naive B cells to conventional memory B cells vs. CD11c+ ABCs (Figure 7E). Naive B cells with top 10 percentile of XIST escape score project strongly into ABC fate (Figure S7E), suggesting that XIST dysregulation may bias this differentiation choice. XIST dysregulation, as reflected by the gain in XIST escape score, is evident in CD11c+ ABCs from female patients but not male patients (Figure 7F), consistent with this being a female-specific phenomenon related to X chromosome dosage. XIST dyregulation in ABCs during COVID-19 infection was replicated in two additional independent patient cohorts (Table S7).

We discovered a similar XIST dysregulation in kidney infiltrating B cells of lupus nephritis and joint tissue infiltrating B cells of rheumatoid arthritis in female patients. In both

cases, CD11c+ ABCs demonstrate significantly higher XIST escape score over conventional memory B cells (Figure 7G-H). Notably, this phenomenon is not observed in B cells from healthy donors, nor female B cells in influenza viral infection, SFTS viral infection, or tumor-infiltrating B cells in breast cancer patients (Table S7). These results suggest that escape of XIST-dependent genes occurs in vivo in several diseases that associated with RNP antigens, and occurs specifically in CD11c+ ABCs that infiltrate the pathologic tissues.

Guided by our single cell trajectory analysis, we hypothesized that XIST dysregulation may promote the differentiation of naive B cells to CD11c+ ABCs. To test this, we deleted XIST in primary human B cells from healthy female donor blood and monitored the B cell differentiation in response to BCR crosslinking and TLR7 stimulation that mimic ssRNA/RNP stimulation. First, we utilized electroporation of Cas9-RNP complex to delete *XIST* A-repeat or *AAVS1* safe harbor locus as control in primary female B cells (Figure 7I; Figure S7F-G). After gating on viable CD19+ B cells (Figure S7H), we found a significant increase of IgD-CD11c+ ABCs in XIST KO group over AAVS1 group (Figure 7J). It is known that TLR7 upregulation can drive the accumulation of CD11c+ atypical B cells (Rubtsov et al., 2011). Indeed, XIST deletion in primary B cells showed ~2.8 fold increase of TLR7 expression compared to AAVS1 group (Figure S7I). TLR7 escape from XCI has been reported to associate with increased IgG class-switching (Souyris et al., 2018). We observed a significant increase of IgG class-switched CD11c+ ABCs after XIST loss (Figure 7K). Our single cell analysis of CD11c+ ABCs showed unique expression pattern including a mixture of IgD-CD27- and IgD-CD27+ populations and higher expression of T-BET and ZEB2 compared to conventional memory cells (Figure S7D). We found that both IgD-CD27-CD11c+ and IgD-CD27+CD11c+ B cell subsets are indeed significantly increased in XIST KO group (Figure S7J-K), and show increased expression of T-BET and ZEB2, key TFs for CD11c+ ABCs (Cancro, 2020) (Figure S7L).

DISCUSSION

Continual requirement for XIST in XCI maintenance of somatic cells

Our study identified a central role of XIST in maintaining X-inactivation in adult human B cells. Classic studies using somatic cell hybrids that deleted the X inactivation center first suggested that XIST is dispensable for XCI maintenance (Brown and Willard, 1994). More recent studies using conditional *Xist* knockout mouse models suggest a range of Xi gene reactivation (Adrianse et al., 2018; Bhatnagar et al., 2014; Yang et al., 2016, 2016; Yildirim et al., 2013). These differences may be due to cell type-specific regulatory mechanism of XCI maintenance, and variable dependency of different X-linked genes on XIST for XCI maintenance. With their substantially longer lifespan than mice, human may be a particularly good model to address the epigenetic memory of XCI maintenance.

X-linked genes lacking promoter DNA methylation are particularly sensitive to XIST loss in B cells. After blocking DNA methylation and H3K27me3, genes classified as XIST-independent become reliant on XIST for XCI maintenance. These data demonstrate that the absence of DNA methylation or other epigenetic memory makes XIST RNA-based transcriptional repression necessary. Thus, our data suggest a redundant model for XCI maintenance: epigenetic memory such as DNA methylation and XIST RNA-based

transcriptional silencing can compensate each other to maintain a robust and durable X-inactivation (Figure 7L). This is in line with a previous study revealing a synergism of XIST RNA and DNA methylation (Csankovszki et al., 2001).

Cell type-specific XIST RNPs to prevent escape from X-inactivation

Our data revealed TRIM28 as a B-cell specific XIST cofactor that is critical to XCI maintenance of a subset of X-linked genes. Since allelic binding of TRIM28 is not enriched at the Xi and there is no direct interaction between TRIM28 and XIST based on UV RIP, we reason that XIST does not directly recruit TRIM28 to the Xi. It is possible that when XIST recruits proteins to spread across the Xi, the XIST RNP comes into contact with TRIM28 that pre-bound at certain loci, leading to indirect interaction between TRIM28 and XIST RNP on chromatin that we detected by CHIRP-MS and RIP experiments with formaldehyde crosslinking. TRIM28 interacts with the A-repeat of XIST, suggesting functional collaboration with other A repeat binding silencing factors such as SPEN and RBM15. Our data suggest two models: (1) TRIM28 acts at promoters while SPEN and other XIST-cofactors act on both enhancers and promoters (Dossin et al., 2020; Żylicz et al., 2019). (2) XIST-RNP regulates the repressor activity of TRIM28. 35% of TRIM28-dependent genes are not dependent on XIST for silencing, favoring the first model. We showed that TRIM28 promoter occupancy is significantly associated with RNA Pol II promoter-proximal pause to cooperate with XIST-mediated H3K27 deacetylation at enhancers, unveiling a regulatory mechanism for XCI maintenance.

The discovery of unique XIST RNPs in somatic cells suggests that different somatic cells can have overlapping but still different XIST co-factors mediated silencing to prevent XCI escape. Like a transcription factor that collaborates with additional transcription coactivators to regulate different target genes in different cell types, the same lncRNA can also recruit, assemble, and guide different protein complexes to enact distinct consequences in different cell types. Studies of somatic cell XIST RNPs should shed light on XCI escape across mammalian organs and cell types.

XIST dysregulation in pathogenic atypical B cells in human disease

Sex is a major determinant of clinical outcomes in autoimmune diseases and COVID-19 and drives different immune responses in men vs. women (Klein and Flanagan, 2016; Takahashi et al., 2020; Williamson et al., 2020). We developed a computational strategy to track XIST dysregulation in any B cell single-cell gene expression data, documenting the in vivo occurrence of escape of XIST-dependent genes in CD11c+ ABCs in multiple diseases. We further experimentally validated that the loss of XIST can facilitate the naive cell differentiation into CD11c+ atypical B cells, providing a first causal link between a known female-enriched B cell population with XIST dysregulation. ABCs exhibits a strong female bias only in aged mice where the hormone difference is minimized, suggesting that XIST-mediated XCI maintenance contributes to the sex dimorphism of this subset (Rubtsov et al., 2011; Rubtsova et al., 2015). Our functional annotation of XIST-silenced genes showed enrichment of the production of IFN-γ which induces the expression of T-BET, a master TF that promotes the differentiation of CD11c+ ABCs upon TLR7 stimulation (Zumaquero et al., 2019). In addition, *CXORF21* is another XIST dependent gene that

encodes a key adaptor protein for TLR7 signaling (Heinz et al., 2020). Therefore, XIST is essential to balance the gene dosage of X-linked immune genes that can greatly impact the formation of CD11c+ ABCs, a rare population in healthy donors but aberrantly expanded in certain infectious diseases and female-biased autoimmune diseases (Cancro, 2020). Future work on how XCI maintenance is impaired in ABCs and other cell types will provide a better understanding of sex dimorphism in human diseases.

Limitations of the Study

In this work, we used genetic ablation of XIST to probe the functions of XIST in XCI maintenance. XIST RNA delocalization is the prevalent phenomenon in B cells of female-biased autoimmunity, and the consequences of XIST delocalization may be more subtle or different than XIST inactivation. We relied heavily on an immortalized B cell line for our epigenomic and mechanistic studies, and futures studies are needed to evaluate these mechanisms in normal B cells in vivo. In addition, our identification of Xi genes requiring XIST maintenance is limited by the available SNPs; denser allelic variants may empower discovery of additional genes requiring this mechanism. Finally, our XIST escape score is based on XIST perturbation in B cells and should only be applied to this cell type. Future studies that illuminate cell type-specific requirements of XIST in XCI maintenance will allow a similar approach to be applied additional cell types in the body.

STAR METHODS

RESOURCE AVAILABILITY

Lead Contact—Further information and requests for resources and reagents should be directed to and will be fulfilled by the Lead Contact, Howard Y. Chang (howchang@stanford.edu).

Materials Availability—The plasmids of TRIM28 mutants with N-terminal 180bp replacement and RING domain or PB domain deletion were available upon request to the Lead Contact.

Data and Code Availability—The accession number for all the sequencing data in this paper is GEO: GSE164596. The mass spectrometry proteomics data have been deposited to the ProteomeXchange Consortium via the PRIDE partner repository with the dataset identifier PXD023516. Details of analysis are provided in STAR methods, and further questions should be directed to the Lead Contact.

EXPERIMENTAL MODEL AND SUBJECT DETAILS

Generation of stable cell lines and cell culture—GM and K562 cell lines were cultured in RPMI 1640 (Thermo Fisher Scientific) with 10% FBS (Thermo Fisher Scientific) and 1% Penicillin-Streptomycin (Gibco). HEK 293T cells were cultured in DMEM (Thermo Fisher Scientific) with 10% FBS and 1% Penicillin-Streptomycin. IMR90 cell line were cultured in EMEM (ATCC) with 10% FBS and 1% Penicillin-Streptomycin. Female mESC were cultured on gelatin-coated plates in N2B27 medium for 7 days and then differentiated into NPC using N2B27 medium supplemented with EGF and FGF (both

10ng/mL, Peprotech). To inhibit DNA methylation and H3K27me3, B cell line was treated with 0.3 uM DNMT inhibitor 5-azacytidine and 2 uM EZH2 inhibitor EPZ-6438 for 7 days.

For generation of XIST CRISPRi GM B cell line, we performed lentiviral transduction of sgXIST in dCas9-KRAB expressing GM B cell line which has been previously made in the lab (Rubin et al., 2019). We designed two sgRNAs targeting the XIST promoter and cloned them into one lentiviral vector as previously described (Rubin et al., 2019). To generate the CRISPRi virus, we cultured HEK 293T cells at 4 million per 10cm dish and transfected with 4.5 ug pMP.G, 1.5 ug psPAX2 and 6 ug sgRNA vector using OptiMEM and Lipofectamin 3000 (Cat# L3000015, Thermo Fisher Scientific) at the following day. Two days later, the supernatant was collected and filtered with 0.44 um filter. The virus was concentrated 1:10 using Lenti-X Concentrator (Clontech). dCas9-KRAB+ GM cells were seeded at 300K cells per well of a 6-well plate and 40 uL concentrated virus was added to the media. Two days later, we select the XIST sgRNA expressing cells by adding 2 ug/mL puromycin for seven days and cells expressing mCherry were sorted by BD Aria II FACS sorter. SETDB1 CRISPRi GM B cell line is generated similarly as XIST CRISPRi GM B cell line.

For generation of anti-CRISPR expressing XIST CRISPRi or control CRISPRi B cell line, we performed lentiviral transduction of anti-CRISPR protein in non-targeting control or XIST (sgXIST) CRISPRi GM B cell line which is generated above. To generate the anti-CRISPR virus, we cultured HEK 293T cells at 4 million per 10cm dish and transfected with 4.5 ug pMP.G, 1.5 ug psPAX2 and 6 ug Fuw-AcrIIA4-P2A-GFP vector (Addgene #108247) using OptiMEM and Lipofectamin 3000 at the following day. Two days later, the supernatant was collected and filtered with 0.44 um filter. The virus was concentrated 1:10 using Lenti-X Concentrator. SgNT or sgXIST CRISPRi cells were seeded at 300K cells per well of a 6-well plate and 40 uL concentrated virus was added to the media. A week later, we select the anti-CRISPR and CRISPRi expressing cells by sorting cells expressing both GFP and mCherry using BD Aria II FACS sorter. The anti-CRISPR efficiency is measured by qRT-PCR of XIST.

For generation of XIST CRISPRi IMR90 cell line, we first established dCas9-KRAB expressing IMR90 cell line by lenti-viral transduction of dCas9-BFP-KRAB (Addgene #46911) and sorted BFP+ cells by BD Aria II FACS sorter. Next, we performed transduction of lentivirus expressing sgXIST or sgNT (non-targeting control) in dCas9-KRAB expressing IMR90 cell line and selected by adding 2 ug/mL puromycin for 7 days and sorted cells expressing both BFP and mCherry. The CRISPRi efficiency is measured by qRT-PCR of XIST.

For generation of TRIM28 CRISPRi K562 cell line, we first established dCas9-KRAB expressing K562 cell line by lenti-viral transduction of dCas9-BFP-KRAB and sorted BFP+ cells by BD Aria II FACS sorter. Next, we performed transduction of lentivirus expressing sgTRIM28 or sgNT in dCas9-KRAB expressing K562 cell line and sorted cells expressing both BFP and mCherry. The CRISPRi efficiency is measured by qRT-PCR of TRIM28.

For generation of XIST A repeat KO GM B cell line, we used CRISPR Cas9 RNP editing to cut XIST A repeat. SgRNAs were produced by combining tracr and crRNA according to the

Synthego Biosciences protocol. Two sgRNAs (30 uM) targeting both ends of XIST repeat A were complexed with 3 ug Cas9 protein (IDT) for 10 min and then electroporated to GM cells (1700V, 20ms, 1 pulse) using Neon Transfection System (Thermo Fisher Scientific). Transfected cells were sorted into 96-well plate for single cell per well and then single cell clone with repeat A deletion was screened by genomic DNA PCR and RT-qPCR.

GM single cell clones with SPEN RRM2-4 deletion were generated similarly as XIST A repeat KO and screened by genomic DNA PCR and RT-qPCR. GM single cell clones with TRIM28 deletion were generated similarly and screened by western blot. All sgRNA sequences were listed in Table S5.

METHOD DETAILS

CHIRP-MS and proteomics analysis—25 T152 flasks of GM12878 or K562 cells were used for ChIRP-MS (0.5–1 billion cells) as previously described (Chu et al., 2015). Cells were cross-linked in 3% formaldehyde for 30 min followed by 0.125 M glycine quenching for 5 min. Cross-linked cells were lysed in fresh NLB buffer (50 mM Tris pH 7.0, 10 mM EDTA, and 1% SDS) and sonicated in 1 mL Covaris tube for 20 min with the following parameters (Fill level:10; Duty Cycle:15; PIP:140; Cycles/burst:200). The supernatant was pre-cleared with streptavidin beads (Invitrogen) and then treated with or without 30 ug/mL Rnase A (Cat # EN0531, Thermo Fisher Scientific) at 37°C for 45 min. Then the supernatant was hybridized with 8.8 uL XIST probes in Hybridization Buffer (50 mM Tris pH 7.0, 1 mM EDTA, 1% SDS, 750 mM NaCl, and 15% Formamide) at 37°C rotating overnight and added with 880uL of streptavidin beads and rotate for 45 min at 37°C. Beads were washed 5 times in ChIRP Wash Buffer (2X SSC and 0.5% SDS) for 5 min at 37°C. RNA extraction can be performed using a small aliquot of post-CHIRP beads to assess the XIST RNA retrieval efficiency. XIST bound proteins were eluted from beads in Biotin Elution Buffer (12.5 mM biotin (Invitrogen), 7.5 mM HEPES, 75 mM NaCl, 1.5 mM EDTA, 0.15% SDS, 0.075% sarkosyl, 15% Formamide, and 0.02% Na-Deoxycholate) at RT for 20 min then shake at 65°C for 10min, finally precipitated by TCA at 4°C overnight. The proteins were pelleted at 16000 rcf at 4°C for 30 min and the protein pellets were washed once with cold acetone and air-dry for 1 min, then the proteins were solubilized in 1X laemmli sample buffer and boiled at 95C for 30 min. Final proteins were size-selected on 4–12% NuPAGE gels for mass spectrometry. Gel slices were excised and diced to 1 mm cubes prior to proteolytic digestion. Samples were reduced in 5 mM DTT in a 50 mM ammonium bicarbonate buffer at 55°C for 30 mins. After removing the residual solvent, proteins were alkylated with 10 mM acrylamide in the same buffer, rinsed with 50% acetonitrile, and then digested using Trypsin-Lys C (Promega) overnight at 37°C to obtain peptides. Samples were centrifuged to condense particulates so that the solvent including peptides could be collected. A further peptide extraction was performed by the addition of 60% acetonitrile, 39.9% water, 0.1% formic acid and incubation for 10–15 min before collection. Samples were dried by speed vac prior to resuspension in 2% aqueous acetonitrile with 0.1% formic acid for mass spectrometry. Mass spectrometry experiments were performed on an Orbitrap Fusion Tribrid mass spectrometer (Thermo Scientific, San Jose, CA) with liquid chromatography using an Acquity M-Class UPLC (Waters Corporation, Milford, MA). For a typical LC/MS experiment, a flow rate of 450 nL/min was used, where mobile

phase A was 0.2% formic acid in water and mobile phase B was 0.2% formic acid in acetonitrile. Analytical columns were pulled and packed in-house using fused silica with an I.D. of 100 microns packed with Dr. Maisch 1.8 micron C18 stationary phase to a length of ~25 cm. Peptides were directly injected onto the analytical column using a gradient (2–45% B, followed by a high-B wash) of 80min. The mass spectrometer was operated in a data-dependent fashion using CID fragmentation for MS/MS spectra generation collected in the ion trap. The collected mass spectra were analyzed using Byonic (Protein Metrics) for peptide identification and protein inference. The search was performed against the Uniprot *homo sapiens* database, including isoforms. Cysteine modified with propionamide was set as a fixed modification in the search, with other typical modifications, *e.g.* oxidation of methionine, included as variable modifications. .Data were held to a 12 ppm mass tolerance for precursors and 0.4 Da for MS/MS fragments, allowing up to two missed cleavage sites. Data were validated using the standard reverse-decoy technique at a 1% false discovery rate. The peptide counts in experiment group and Rnase treatment group for each replicate in GM and K562 cells are listed in Table S3. The XIST binding proteins were first identified in each replicate with peptide counts >25 and fold enrichment (experiment group/Rnase treatment group) >1.5. Then the proteins that are overlapped between replicates were identified and further filtered using mean fold enrichment from two replicates>2.5. The highly-confident XIST binding proteins for CRISPRi screen were identified using peptide counts>25 and mean fold enrichment >10.

RNA immunoprecipitation (UV-RIP and formaldehyde-RIP)—The RNA immunoprecipitation protocol was performed as previously described (G Hendrickson et al., 2016) with a few modifications. For UV-RIP, 5 million cells per replicate were crosslinked by UV exposure at 0.3 J/cm2 (254nM UV-C). For formaldehyde-RIP (fRIP), 5 million cells per replicate were fixed in 0.1% formaldehyde for 10 min at RT and quenched by 0.125 M glycine for 10 min at RT. UV-crosslinked or formaldehyde-fixed cells were washed by cold PBS and lysed in lysis buffer (50 mM Tris, 150 mM Kcl, 0,1% SDS, 1% Triton-X, 5 mM EDTA, 0.5% sodium deoxycholate, 0.5 mM DTT, 1XPIC, 100 U/mL RNAseOUT inhibitor) and sonicated using a Covaris Ultrasonicator tube (140W, 10% duty cycle, 200cycles/burst). After 15 min max speed spin at 4°C, the supernatant was pre-cleared with Protein A/G beads for 30 min at 4°C and the beads were disposed. An aliquot of the supernatant was saved as the total input control. The leftover supernatant was incubated with 2 ug mouse IgG (Thermo Fisher) or 2 ug KAP1 (ab10483, Abcam) and rotated overnight at 4°C. 20ul Protein A/G beads were added and rotated for 2 h at 4°C and washed four times with native lysis buffer (25 mM Tris, 150 mM KCl, 5 mM EDTA, 0.5% NP-40, 1X PIC, 100 U/mL RNAseOUT inhibitor, 0.5 mM DTT). The IP beads and input samples were reverse-crosslinked in RCL buffer (2% N-lauroyl Sarcosine, 10 mM EDTA, 5 mM DTT in PBS without Mg and Ca) with Proteinase K and RNAseOUT inhibitor for 1h at 42°C and then another 1h at 50°C, shaking at 1000 rpm. The RNA was purified using Quick-RNA Miniprep Kit (Zymo Research). The RNA quality was checked by BioAnalyzer and the qRT-PCR was performed using Stratagene Brilliant II SYBR Green QRT-PCR Master Mix (Agilent). The primers for RIP qPCR were listed in Table S6.

RNA extraction, RT-qPCR, and pyrosequencing—RNA was extracted in TRIzol using Quick-RNA Miniprep Kit following the manufacturer's protocol with on-column Dnase digestion (Zymo Research). RT-qPCR was performed using Stratagene Brilliant II SYBR Green QRT-PCR Master Mix (Agilent). To quantify the allelic bias, cDNA was generated by reverse transcription of extracted RNA using SuperScriptIII and the amplified for 5 cycles using targeted qPCR primers. Then the PCR product was purified by Zymo DNA Clean & Concentrator-5 and further amplified using biotinylated primers and sequenced on using Q24 Pyromark (Qiagen). All primers for qRT-PCR and pyrosequencing are listed in Table S6.

RNA-seq—RNA was extracted using Quick-RNA Miniprep Kit with on-column Dnase digestion (Zymo Research). At least 100ng RNA was used to prepare the RNA-seq library using TruSeq® Stranded mRNA Library Prep Kit (Cat# 20020594, Illumina) for each sample following the manufacturer's instruction. The library was sequenced on an Illumina Hiseq 4000 to generate 2X75 paired-end reads or 2X150 paired-end reads.

Rescue experiment with TRIM28 mutants—Since TRIM28 KO B cells are lethal, we developed a strategy to first express TRIM28 mutants and then knock out the endogenous TRIM28. Lentiviral vectors that carry full length TRIM28 and RING domain or PB (PHD-Bromodomain) domain deletion mutants conjugated to eGFP fused with a 2A peptide were cloned using Gibson Assembly from the PCR product of the plasmid containing TRIM28 cDNA (Addgene #124960). The N-terminal 180 bp sequence of all TRIM28 variants was altered to distinguish with endogenous TRIM28 sequence with silent mutation (producing same amino acids with endogenous TRIM28). Lentivirus expressing TRIM28 mutants were made similarly as above. B cells were transduced with TRIM28 mutants expressing lentivirus for 5 days and GFP^{hi} cells were sorted for endogenous TRIM28 knockout. Two sgRNAs (30 uM) targeting the sequence inside of the N-terminal 180 bp of endogenous TRIM28 were complexed with 3 ug Cas9 protein (IDT) for 10 min and then electroporated to GFP^{hi} B cells (1700V, 20ms, 1 pulse) using Neon Transfection System. The knockout efficiency was measured by indel from sanger sequencing of genomic DNA PCR product of the first 180bp. The percentage of indels was calculated by ICE analysis (Synthego).

CUT&RUN

CUT&RUN for H3K27me3 and H3K9me3 were performed as previously described in (Skene and Henikoff, 2017). Briefly, 0.5 million cells per replicate were bound to 10 uL concanavalin A-coated beads (Cat# BP531, Bangs Laboratories) in Binding Buffer (20 mM HEPES, 10 mM KCl, 1 mM CaCl2 and 1 mM MnCl2). The beads were washed and resuspended in Dig-Wash Buffer (20 mM HEPES, 150 mM NaCl, 0.5 mM Spermidine, 0.05% Digitonin, and 1X PIC). The primary antibody of H3K27me3 (Ab6002, Abcam, 1ug) or H3K9me3 (Ab8898, Abcam, 1ug) was added to the bead slurry and rotated at 4°C overnight. The beads were washed by Dig-Wash Buffer and the secondary antibody (1:50 for rabbit anti-mouse IgG) was added and rotated at 4°C for 1 h, and washed by Dig-Wash buffer. The pA-Mnase fusion protein (a gift from Henikoff lab) was added at 700ng/mL and rotated at 4°C for 1 h. Next, the beads were washed by Dig-Wash buffer twice followed by Low-Salt Rinse Buffer (50 mM HEPES and 0.02% Digitonin). The targeted

digestion was performed by incubating at 0°C in Incubation Buffer (3.5 mM HEPES, 10 mM CaCl2, and 0.02% Digitonin) for 30 min and stopped by 1X STOP buffer (20 mM EGTA, 0.02% Digitonin, 25 ug/mL RnaseA, 50 ug/mL Glycogen, and 170mM NaCl). The chromatin was released by incubating at 37°C for 30 min. The DNA extraction was performed by NucleoSpin Gel and PCR Clean-up kit (Cat# 740609.250, Machery-Nagel). The CUT&RUN library was prepared using NEBNext Ultra II DNA library prep kit for Illumina (NEB) following the manufacturer's protocol, and finally sequenced on an Illumina Hiseq 4000 to generate 2X75 paired-end reads.

ChIP-seq—For H3K27ac ChIP-seq, 1 million cells per replicate were fixed in 1% formaldehyde for 10 min at RT and quenched by 0.125 M glycine for 10 min at RT. For Trim28 ChIP-seq, 1 million cells per replicate were first cross-linked with 2 mM DSG for 40 min at RT and then fixed in 1% formaldehyde for 10 min at RT and finally quenched by 0.125 M glycine for 10 min at RT. Fixed cells were first lysed in membrane lysis buffer (50 mM HEPES-KOH, 140 mM NaCl, 1 mM EDTA, 10% glycerol, 0.5% NP-40, 0.25% TritonX-100) for 10 min at 4°C. Then pelleted nuclei were lysed in nuclear lysis buffer (10mM Tris, 200mM NaCl, 1mM EDTA, 0.5mM EGTA) for 10min at RT. The chromatin was resuspended in Covaris sonication buffer (10 mM Tris, 1 mM EDTA, 0.1% SDS) and sonicated in a Covaris Ultrasonicator milliTube (140W, 10% duty cycle, 200 cycles/burst) to get 150–700bp length. The sonicated lysate was incubated with 4 ug H3K27ac (ab4729, Abcam) or 5 ug KAP1 (ab10483, Abcam) overnight at 4°C. Antibody-bound chromatin was incubated with Protein-G Dnyabeads (10004D, Invitrogen) for 4 h at 4°C and washed five times with RIPA wash buffer (5 mM HEPES-KOH, 500 mM LiCl, 1 mM EDTA, 1% NP40, 0.7% Sodium Deoxycholate) and eluted in elution buffer (10 mM Tris, 10 mM EDTA, 1% SDS). The eluted sample was incubated at 65°C overnight to reverse the crosslink and treated with RNAse A for 1h at 37°C and Proteinase K for 1h at 55°C. DNA was extracted using ChIP DNA Clean & Concentrator kit (Zymo Research). The ChIP-seq library was prepared using NEBNext Ultra II DNA library prep kit for Illumina (NEB) following the manufacturer's protocol, and finally sequenced on an Illumina Hiseq 4000 to generate 2X 75 paired-end reads.

CRISPRi screen for allelic expression of TLR7—We designed two sgRNAs per XIST co-factor gene with each targeting a different region in 200 bp after the transcriptional start site using CRISPOR. One sgRNA each was cloned into pMJ117 (human U6 vector) or pMJ179 (mouse U6 vector) which were digested with BstXI and BlpI using NEBuilder HiFi DNA Assembly Master Mix (NEB). Then the corresponding U6 promoter and sgRNA sequences were PCR amplified and cleaned up by ZR-96 DNA Clean & Concentrator-5 (Deep Well). The PCR fragments were assembled into the pU6-sgGFP-NT1 lentiviral vector which was digested with XbaI and XhoI, using NEBuilder HiFi DNA Assembly Master Mix. Finally, the individual colonies with 2X sgRNA plasmid were screened by colony PCR and confirmed by Sanger sequencing. To generate CRISPRi lentivirus, we plated 800K HEK293T cells per well for 6-well pate and for the next day we transfected 0.75 ug pMP.G, 0.25 ug psPAX2, and 1 ug sgRNA vector in 100 uL Opti-MEM using Lipofectamin 3000. After two days, the supernatant was collected and the virus was concentrated 1:10 using Lenti-X Concentrator (Clontech). 200K dCas9-KRAB expressed GM cell line were plated

per well in 24 well plates and 40 uL concentrated virus was added the following day. Two days later, we select the Xist-cofactor sgRNA expressing cells by adding 2 ug/mL puromycin for 2–3 weeks. Selection media was refreshed every three days. RNA was extracted using Direct-zol-96 RNA Kit (Zymo Research). TLR7 RT-PCR was performed using Stratagene Brilliant II SYBR Green QRT-PCR Master Mix (50°C for 30 min, 95°C for 10 min, then 35 cycles of 95°C for 30 seconds, 60°C for 1 min, and 72°C for 30 seconds, finally 72°C for 5 min). The second PCR with Ad1_TLR7_F and Ad2_TLR7_R primers was performed using NEBNext Master Mix (2.5uL 1^{st} PCR product with 500 nM primers in program: 98°C for 1 min, 20 cycles of 98°C for 30 seconds, 60°C for 30 seconds, and then 72°C for 40 seconds, finally 72°C for 5 min). The third PCR with indexed primers containing barcodes was performed using NEBNext Master Mix (2uL of 1:10 diluted 2^{nd} PCR product with 1uM indexed primers in program: 98°C for 1 min, 10 cycles of 98°C for 30 seconds, 72°C for 30 seconds, and then 72°C for 40 seconds, finally 72°C for 5 min). Finally, all the samples were pooled and purified using Zymo DNA clean & concentrator. The library was size-selected to 250–300 bp. The gel slices were cut and the DNA was recovered by Zymo Gel DNA recovery kit (Zymo Research). The concentration of the library was quantified by KAPA Library Quantification Kit for Illumina (Roche) and sequenced on an Illumina Miseq 2X75 cycle. Reads were mapped directly to TLR7 reference Xa and Xi allele and counted at each allele for d-score analysis. The co-factors with $\text{d-score}^{\text{co-factor}}$ -$\text{d-score}^{\text{Ctrl}}$ >0.1 were labeled as essential XIST co-factors for TLR7 XCI maintenance.

Human primary B cell editing with Cas9 RNP—Buffy coats from female healthy donors were obtained from Stanford Blood Center with consent forms. Peripheral blood mononuclear cells (PBMC) were isolated using Lymphoprep (Cat# 07811, STEMCELL Technologies) density-gradient centrifugation and cryopreserved and stored in −80C. B cells were purified from thawed PBMCs by negative selection using EasySep Human B Cell Enrichment Kit (Cat#19844, STEMCELL Technologies) following the manufacturer's protocol. Isolated B cells were cultured in IMDM medium supplemented with 10% FBS and 55 mM beta-mercaptoethanol at $1X10^6$ cell/mL and primed with CellXVivo Human B cell expander (1:250 dilution, R&D system), 50 ng/mL IL10 (Cat#200-10-2ug, PeproTech), 10 ng/mL IL15 (Cat#200-15-2ug, PeproTech), 50 ng/mL IL2 (Cat#200-02-10ug, PeproTech) for two days. For B cell electroporation, primed B cells were washed by PBS twice and resuspended in Neon Buffer T (Cat# MPK1025, Thermo Fisher Scientific). Two sgRNAs (30 uM) targeting both ends of XIST repeat A were complexed with 3 ug Cas9 protein (IDT) for 10 min at RT. Cas9 RNP was added to the resuspension to get the final cell density at 3 X10^7 cells/ml and the electroporation was performed (1700V, 20ms, 1pulse) in 10 uL Neon transfection system. Electroporated cells were immediately transferred to pre-warmed B cell expansion medium (RPMI 1640 +10% FBS +1XGlutaMAX (Thermo Fisher Scientific) + 50 ng/mL IL2 + CellXVivo Human B cell expander (1:250 dilution, R&D system)). After two days of culture, an aliquot of cells was saved to test editing efficiency. The left cells were activated in B cell expansion medium supplemented with 1 ug/mL TLR7 agonist R848 (Invivogen) and 5 ug/mL F'2 Fragment Goat Anti-Human IgM (Cat# C840J42, Jackson ImmunoResearch Laboratories) for 5 days and subjected to flow cytometry.

Flow cytometry—B cells were first incubated with Human TruStain FcXTM (Fc Block, BioLegend) in cell staining buffer (Biolegend, Cat# 420201) for 30 min on ice and then stained with viability dye (Thermo Fisher, Cat # R37610), CD27 (clone O323), IgD (clone IA6-2), IgG(clone G18–145), CD19 (clone HIB19), and CD11c (clone Bu15) for 20 min on ice. The stained cells were washed in 1X FACS buffer for twice and are ready for flow cytometry. All flow cytometry antibodies are from Biolegend or BD Biosciences. All flow cytometry was performed using LSRII and FACS data were analyzed by FlowJo.

Computational analysis for RNA-seq—RNA-seq reads were mapped to the human genome (hg19) using STAR with default parameters (--outFilterMultimapNmax 1 --alignEndsType EndToEnd --outSAMattributes NH HI NM MD). Mitochodria reads were removed by samtools and duplicated reads were removed by picard. Quantification of aligned reads at the gene level was performed by HTseq count with default parameters (--stranded=reverse –additional-attr=gene_name). Raw counts were used to identify differentially expressed genes (DEG) using DESeq2 with size factor (total reads) normalization and DEGs were identified if Benjamini & Hochberg adjusted p-value <0.05. For Gene Ontology (GO) term analysis in Figure S1H, PANTHER GO was used. For gene functional annotation in Figure 7A, DAVID gene-annotation enrichment, KEGG pathway, and GAD disease category were used with cut-off (Benjamini & Hochberg adjusted p-value < 0.05 and fold enrichment > 3). In Figure 7, GSEA analysis was performed using Genepattern GSEA module with public available female SLE PBMC and B cell subset RNA-seq data (Jenks et al., 2018; Tokuyama et al., 2018). The gene sets used in GSEA analysis (genes upregulated in sgXIST, XIST-dependent X-linked genes, and XIST-independent X-linked genes) were listed in Table S2.

For allelic-specific RNA-seq analysis, SNP sites for donor NA12878 were extracted from the dbSNP database. SNP sites that are shared between paternal and maternal alleles but different from the human genome were kept as the common NA12878 SNP. SNP sites that are different between paternal and maternal allele were replaced by ‘N’ to build up N-masked reference genome. To maximize the allelic read depth, two biological replicates were pooled for later analysis. RNA-seq reads were aligned to the N-masked reference genome by STAR. After alignment and removal of mitochondria reads, remaining reads were split to maternal-specific (Xa) or paternal-specific (Xi) allele using SNPsplit. Duplicated reads were removed by picard and quantification of allele-specific reads at the gene level was performed via htseq-count similar to the bulk analysis. Genes with allelic reads >10 were retained to calculate the d-score ($reads^{Xi}/(reads^{Xa}+reads^{Xi})-0.5$). For genes with d-score <0, genes with $d\text{-}score^{sgXIST}$-$d\text{-}score^{ctrl}$ > 0.03 and binomial P value <0.05 are defined as XIST-dependent genes. The other genes are XIST-independent genes. X-linked immune gene set was curated from review (Libert et al., 2010). The hierarchical clustering was performed using seaborn clustermap with parameters (metric=euclidean, z_score=0). In Figure S1G, the variable escapee, constitutive escapee and the X-inactivated genes were defined from GTEx study (Tukiainen et al., 2017). In Figure S2C-D, the effect size of sex bias for variable escapees in different tissues and the category of variable escapee, constitutive escapee, and the X-inactivated genes were defined from GTEx study (Oliva et al., 2020). In Figure 6, genes with $d\text{-}score^{TRIM28KO}$-$d\text{-}score^{ctrl}$ > 0.03 and $d\text{-}score^{ctrl}$ <0

are defined as TRIM28-dependent genes. The other genes with d-score^{ctrl} <0 are defined as TRIM28-independent genes. Bedgraph files were generated from bam files using bedtools genomcov and then convert to bigwig files for IGV visualization.

Computational analysis for CUT&RUN and ChIP-seq—Reads were mapped to the human genome (hg19) using bowtie2 with default parameters (--very-sensitive). Mitochondrial reads were removed by samtools and duplicated reads were removed by picard. For allelic-specific analysis, to maximize the allelic read depth, two biological replicates were pooled for later analysis. Reads were aligned to the N-masked reference genome by bowtie2. After alignment and removal of mitochondria reads and duplicated reads, remaining reads were split to Xa or Xi allele using SNPsplit. For ChIP-seq of H3K27ac, peaks were called using MACS2 with parameters (--broad -f BAMPE –broad-cutoff 0.01) over input control. The total consensus peak coordinate across samples was obtained using bedtools merge and intersect. The peaks were assigned to the nearest genes using HOMER annotatePeaks. The peaks within TSS +/− 1kb range were defined as promoters and other distal H3K27ac peaks were defined as enhancers. Allelic reads overlapping on peaks were counted using bedtools intersect and peaks with the allelic reads >10 were retained to calculate the d-score (reads^{Xi}/(reads^{Xa}+reads^{Xi})-0.5). For H3K27me3 and H3K9me3 CUT&RUN and TRIM28 ChIP-seq, reads were aligned and filtered as above. TRIM28 ChIP-seq in K562 cell line is downloaded from public ENCODE dataset ENCFF165QYW. The windows were binned as TSS adjacent regions (TSS +/− 1kb) and gene bodies (TSS+1kb to TES) for each gene. Total and allelic reads overlapping these regions were counted using bedtools and regions with the allelic reads >10 were retained to calculate the d-score. Average plot of TRIM28 bulk signal was generated by ngsplot. Bedgraph files were generated from bam files using bedtools genomcov and then convert to bigwig files for IGV visualization.

Feature comparison—ChIP-seq of H3K27ac (ENCFF180LKW), RNA Pol II (ENCFF368HBX), Ser5P RNA Pol II (ENCFF002UPS), and Ser2P RNA Pol II (ENCFF031RUV), MEDIP-seq (GSE56774)(Sundaram et al., 2014), and GRO-seq (GSE60454)(Core et al., 2014) from public available ENCODE and GEO datasets were used for feature comparison. ATAC-seq of GM12878 cells (Buenrostro et al., 2013) and our CUT&RUN of H3K9me3 and H3K27me3 in control GM cells were used for feature comparison. Reads were aligned to hg19 or N-masked hg19 genome by bowtie2 with mitochondria reads and duplicated reads removal as above. The windows were binned as TSS adjacent regions (TSS +/− 1kb) and gene bodies (TSS+1kb to TES) for each gene. Total and allelic reads overlapping these regions were counted using bedtools and regions with the allelic reads >10 were retained to calculate the d-score. GC content was calculated by bedtools nuc. CpG island, LINE, SINE, and LTR files were downloaded from UCSC Table browser (RepeatMasker) and their density at TSS adjacent regions or gene bodies were counted by bedtools. For linear regression analysis, counts of each feature across X-linked genes were scaled from 0 to 1 individually and analysis was performed by statsmodels linear regression with OLS model. For logistical regression analysis, train and test sets for features were split by sklearn train_test_split with test_size=0.25. Then analysis was performed using sklearn LogisticRegression. GRO-seq analysis was performed using

HOMER. The promoter-proximal index was calculated as read density$^{\text{TSS adjacent regions}}$/read density$^{\text{gene bodies}}$ for each X-linked gene.

Computational analysis for single-cell RNA-seq—Public single-cell RNA-seq data were downloaded from GEO database (GSE149689(Lee et al., 2020), GSE154567(Yao et al., 2021), GSE155673(Arunachalam et al., 2020), GSE142016(Mistry et al., 2019), GSE159117(Zhang et al., 2020), GSE149313, GSE145281(Yuen et al., 2020), GSE135710(Lu et al., 2020)) and ImmPort repository (SDY997(Arazi et al., 2019), SDY998(Zhang et al., 2019)). The single cell data preprocess is done by Scanpy version 1.4.6 (Wolf et al., 2018). The sex of the sample is validated by the expression of male-specific gene DDX3Y, and female-specific gene XIST. The genes that are detected in less than 3 cells were removed using sc.pp.filter_genes(). The cells with fewer than 200 detected genes and higher than 10% mitochondrial genes were removed. The data was normalized to 10000 reads per cell for total-count to correct the library size using sc.pp.normalize_total() with target_sum=1e4. The data was then log transformed using sc.pp.log1p(). The top 2000 highly-variable genes were identified using sc.pp.highly_variable_genes() with min_mean=0.0125, max_mean=3, min_disp=0.5. The total counts per cell and the percentage of mitochondrial genes expressed were regressed out using sc.pp.regress_out(). Each gene is scaled to unit variance using sc.pp.scale() with max_value=10. Principle component analysis was performed using top 2000 highly variable genes using sc.tl.pca(). Then the top 40 principle components were used to compute the neighborhood graph for dimensional reduction using sc.pp.neighbors() with n_neighbors=10, n_pcs=40, random_state=1. The Leiden graph-clustering method was applied to find Leiden clusters using sc.tl.leiden() with different resolution based on datasets. The B cell clusters were subset based on B cell marker genes MS4A1 and CD79A while excluding other immune cell types based on cell-specific marker genes such as CD3E, CD14, PPBP, CD4, CD8A, FCER1A, and CST3 etc. The clusters for B cell subsets were manually annotated as naive, conventional memory, atypical memory B cells based on known cell type markers (IGHD, IGHG1, CD27, ITGAX). The UMAP plots on these marker genes for B cell subsets were generated by sc.tl.umap() and sc.pl.umap(). The compact violin plot for more marker genes of these B cell subsets was generated by sc.pl.stacked_violin(). For XIST escape score analysis, the score is calculated by mean expression of XIST-dependent X-linked genes subtract mean expression of XIST-independent X-linked genes (gene sets from Table S2). The calculation is performed using sc.tl.score_genes() with XIST-independent genes as reference gene pool and XIST-dependent genes as target gene list (ctrl_size=50, n_bins=25). The p value of gene score between subsets was calculated by unpaired t-test using scipy stats ttest_ind() function. For trajectory analysis, a weighted nearest neighbor graph was first constructed t0 build a transition matrix by sc.pp.neighbors() with n_neighbors=20, method=‘gauss’. Then the naive B cell is assigned as a root cell. The diffusion map was computed using n_comps=15 by sc.tl.diffmap(). The Diffusion Pseudotime order was computed by sc.tl.dpt() with n_branchings=1, n_dcs=10 to identify branching point and differentiation endpoint. The diffusion pseudotime plot was generated by sc.pl.diffmap().

QUANTIFICATION AND STATISTICAL ANALYSES

Statistical analyses are performed by Python and R. Information on specific statistical tests are listed in the figure legends and/or method details. Data are represented by mean+/−SEM in bar plots as indicated in the figure legends. P values are listed on figures or figure legends.

Supplementary Material

Refer to Web version on PubMed Central for supplementary material.

ACKNOWLEDGEMENT

We thank CK. Chen, K.L. Huang, N. Pacalin, A. Carter, J. Xu, members of the Chang lab and E. Heard for discussion. We also thank R. Leib at Mass Spectrometry core, PAN facility, FACS facility and SFGF sequencing core at Stanford University. Supported by Scleroderma Research Foundation, Pershing Square Foundation, NIH U54-CA260517, NIH RM1-HG007735 (to H.Y.C.), and a Stanford Dean's Fellowship (to B.Y.). A.T.S. was supported by the NIH (K08CA230188 and U54260517), a Career Award for Medical Scientists from the Burroughs Wellcome Fund, Fast Grants from Emergent Ventures, and Stanford's Innovative Medicine Accelerator and Stanford ChEM-H. H.Y.C. is an Investigator of the Howard Hughes Medical Institute.

REFERENCES

Adrianse RL, Smith K, Gatbonton-Schwager T, Sripathy SP, Lao U, Foss EJ, Boers RG, Boers JB, Gribnau J, and Bedalov A (2018). Perturbed maintenance of transcriptional repression on the inactive X-chromosome in the mouse brain after Xist deletion. Epigenetics Chromatin 11, 50. [PubMed: 30170615]

Almeida M, Bowness JS, and Brockdorff N (2020). The many faces of Polycomb regulation by RNA. Curr. Opin. Genet. Dev. 61, 53–61. [PubMed: 32403014]

Anders S, Pyl PT, and Huber W (2015). HTSeq—a Python framework to work with high-throughput sequencing data. Bioinformatics 31, 166–169. [PubMed: 25260700]

Arazi A., Rao DA., Berthier CC., Davidson A., Liu Y., Hoover PJ., Chicoin A., Eisenhaur TM., Jonsso AH., L S., et al. . (2019). The immune cell landscape in kidneys of patients with lupus nephritis. Nat. Immunol. 20, 902–914. [PubMed: 31209404]

Arunachalam PS, Wimmers F, Mok CKP, Perera RAPM, Scott M, Hagan T, Sigal N, Feng Y, Bristow L, Tak-Yin Tsang O, et al. (2020). Systems biological assessment of immunity to mild versus severe COVID-19 infection in humans. Science 369, 1210–1220. [PubMed: 32788292]

Bhatnagar S, Zhu X, Ou J, Lin L, Chamberlain L, Zhu LJ, Wajapeyee N, and Green MR (2014). Genetic and pharmacological reactivation of the mammalian inactive X chromosome. Proc. Natl. Acad. Sci. U. S. A. 111, 12591–12598. [PubMed: 25136103]

Brown CJ, and Willard HF (1994). The human X-inactivation centre is not required for maintenance of X-chromosome inactivation. Nature 368, 154–156. [PubMed: 8139659]

Buenrostro JD, Giresi PG, Zaba LC, Chang HY, and Greenleaf WJ (2013). Transposition of native chromatin for multimodal regulatory analysis and personal epigenomics. Nat. Methods 10, 1213–1218. [PubMed: 24097267]

Cancro MP (2020). Age-Associated B Cells. Annu. Rev. Immunol. 38, 315–340. [PubMed: 31986068]

Carrel L, and Brown CJ (2017). When the Lyon(ized chromosome) roars: ongoing expression from an inactive X chromosome. Philos. Trans. R. Soc. Lond. B. Biol. Sci. 372.

Carter AC, Xu J, Nakamoto MY, Wei Y, Zarnegar BJ, Shi Q, Broughton JP, Ransom RC, Salhotra A, Nagaraja SD, et al. (2020). Spen links RNA-mediated endogenous retrovirus silencing and X chromosome inactivation. ELife 9.

Celhar T, Magalhães R, and Fairhurst A-M (2012). TLR7 and TLR9 in SLE: when sensing self goes wrong. Immunol. Res. 53, 58–77. [PubMed: 22434514]

Christensen SR, Shupe J, Nickerson K, Kashgarian M, Flavell RA, and Shlomchik MJ (2006). Toll-like receptor 7 and TLR9 dictate autoantibody specificity and have opposing inflammatory and regulatory roles in a murine model of lupus. Immunity 25, 417–428. [PubMed: 16973389]

Chu C, Zhang QC, da Rocha ST, Flynn RA, Bharadwaj M, Calabrese JM, Magnuson T, Heard E, and Chang HY (2015). Systematic discovery of Xist RNA binding proteins. Cell 161, 404– 416. [PubMed: 25843628]

Core LJ, Martins AL, Danko CG, Waters CT, Siepel A, and Lis JT (2014). Analysis of nascent RNA identifies a unified architecture of initiation regions at mammalian promoters and enhancers. Nat. Genet. 46, 1311–1320. [PubMed: 25383968]

Csankovszki G, Panning B, Bates B, Pehrson JR, and Jaenisch R (1999). Conditional deletion of Xist disrupts histone macroH2A localization but not maintenance of X inactivation. Nat. Genet. 22, 323–324. [PubMed: 10431231]

Csankovszki G, Nagy A, and Jaenisch R (2001). Synergism of Xist RNA, DNA methylation, and histone hypoacetylation in maintaining X chromosome inactivation. J. Cell Biol. 153, 773–784. [PubMed: 11352938]

Czerwińska P, Mazurek S, and Wiznerowicz M (2017). The complexity of TRIM28 contribution to cancer. J. Biomed. Sci. 24, 63. [PubMed: 28851455]

Dobin A, and Gingeras TR (2015). Mapping RNA-seq Reads with STAR. Curr. Protoc. Bioinforma. 51, 11.14.1–11.14.19.

Dossin F., Pinheiro I., Żylicz JJ., Roensch J., Collombet S., Le Saux A., Chelmicki T., Attia M., Kapoor V., Zhan Y., et al. . (2020). SPEN integrates transcriptional and epigenetic control of X-inactivation. Nature 578, 455–460. [PubMed: 32025035]

ENCODE Project Consortium (2012). An integrated encyclopedia of DNA elements in the human genome. Nature 489, 57–74. [PubMed: 22955616]

G Hendrickson D, Kelley DR, Tenen D, Bernstein B, and Rinn JL (2016). Widespread RNA binding by chromatin-associated proteins. Genome Biol. 17, 28. [PubMed: 26883116]

Gartler SM, and Riggs AD (1983). Mammalian X-chromosome inactivation. Annu. Rev. Genet. 17, 155–190. [PubMed: 6364959]

Hao Y, O'Neill P, Naradikian MS, Scholz JL, and Cancro MP (2011). A B-cell subset uniquely responsive to innate stimuli accumulates in aged mice. Blood 118, 1294–1304. [PubMed: 21562046]

Hasegawa Y, Brockdorff N, Kawano S, Tsutui K, Tsutui K, and Nakagawa S (2010). The matrix protein hnRNP U is required for chromosomal localization of Xist RNA. Dev. Cell 19, 469–476. [PubMed: 20833368]

Heinz LX, Lee J, Kapoor U, Kartnig F, Sedlyarov V, Papakostas K, César-Razquin A, Essletzbichler P, Goldmann U, Stefanovic A, et al. (2020). TASL is the SLC15A4-associated adaptor for IRF5 activation by TLR7–9. Nature 581, 316–322. [PubMed: 32433612]

Heinz S, Benner C, Spann N, Bertolino E, Lin YC, Laslo P, Cheng JX, Murre C, Singh H, and Glass CK (2010). Simple combinations of lineage-determining transcription factors prime cis-regulatory elements required for macrophage and B cell identities. Mol. Cell 38, 576–589. [PubMed: 20513432]

Hoki Y, Kimura N, Kanbayashi M, Amakawa Y, Ohhata T, Sasaki H, and Sado T (2009). A proximal conserved repeat in the Xist gene is essential as a genomic element for X-inactivation in mouse. Development 136, 139–146. [PubMed: 19036803]

Iyengar S, and Farnham PJ (2011). KAP1 Protein: An Enigmatic Master Regulator of the Genome. J. Biol. Chem. 286, 26267–26276. [PubMed: 21652716]

Jenks SA, Cashman KS, Zumaquero E, Marigorta UM, Patel AV, Wang X, Tomar D, Woodruff MC, Simon Z, Bugrovsky R, et al. (2018). Distinct Effector B Cells Induced by Unregulated Toll-like Receptor 7 Contribute to Pathogenic Responses in Systemic Lupus Erythematosus. Immunity 49, 725–739.e6. [PubMed: 30314758]

Karnell JL, Kumar V, Wang J, Wang S, Voynova E, and Ettinger R (2017). Role of CD11c+ T-bet+ B cells in human health and disease. Cell. Immunol. 321, 40–45. [PubMed: 28756897]

Klein SL, and Flanagan KL (2016). Sex differences in immune responses. Nat. Rev. Immunol. 16, 626–638. [PubMed: 27546235]

Krueger F, and Andrews SR (2016). SNPsplit: Allele-specific splitting of alignments between genomes with known SNP genotypes. F1000Research 5, 1479. [PubMed: 27429743]

Langmead B, and Salzberg SL (2012). Fast gapped-read alignment with Bowtie 2. Nat. Methods 9, 357–359. [PubMed: 22388286]

Lee JS., Park S., Jeong HW., Ahn JY., Choi SJ., Lee H., Choi B., Nam SK., Sa M., Kwon J-S., et al. . (2020). Immunophenotyping of COVID-19 and influenza highlights the role of type I interferons in development of severe COVID-19. Sci. Immunol. 5.

Li H, Handsaker B, Wysoker A, Fennell T, Ruan J, Homer N, Marth G, Abecasis G, Durbin R, and 1000 Genome Project Data Processing Subgroup (2009). The Sequence Alignment/Map format and SAMtools. Bioinforma. Oxf. Engl. 25, 2078–2079.

Libert C, Dejager L, and Pinheiro I (2010). The X chromosome in immune functions: when a chromosome makes the difference. Nat. Rev. Immunol. 10, 594–604. [PubMed: 20651746]

Loda A, and Heard E (2019). Xist RNA in action: Past, present, and future. PLOS Genet. 15, e1008333.

Love MI, Huber W, and Anders S (2014). Moderated estimation of fold change and dispersion for RNA-seq data with DESeq2. Genome Biol. 15, 550. [PubMed: 25516281]

Lu Y, Zhao Q, Liao J-Y, Song E, Xia Q, Pan J, Li Y, Li J, Zhou B, Ye Y, et al. (2020). Complement Signals Determine Opposite Effects of B Cells in Chemotherapy-Induced Immunity. Cell 180, 1081–1097.e24. [PubMed: 32142650]

Lu Z, Zhang QC, Lee B, Flynn RA, Smith MA, Robinson JT, Davidovich C, Gooding AR, Goodrich KJ, Mattick JS, et al. (2016). RNA Duplex Map in Living Cells Reveals Higher-Order Transcriptome Structure. Cell 165, 1267–1279. [PubMed: 27180905]

Lu Z, Carter AC, and Chang HY (2017). Mechanistic insights in X-chromosome inactivation. Philos. Trans. R. Soc. Lond. B. Biol. Sci. 372.

Lyon MF (1962). Sex Chromatin and Gene Action in the Mammalian X-Chromosome. Am. J. Hum. Genet. 14, 135–148. [PubMed: 14467629]

Ma X, Yang T, Luo Y, Wu L, Jiang Y, Song Z, Pan T, Liu B, Liu G, Liu J, et al. (2019). TRIM28 promotes HIV-1 latency by SUMOylating CDK9 and inhibiting P-TEFb. ELife 8.

McHugh CA, Chen C-K, Chow A, Surka CF, Tran C, McDonel P, Pandya-Jones A, Blanco M, Burghard C, Moradian A, et al. (2015). The Xist lncRNA interacts directly with SHARP to silence transcription through HDAC3. Nature 521, 232–236. [PubMed: 25915022]

Minajigi A, Froberg J, Wei C, Sunwoo H, Kesner B, Colognori D, Lessing D, Payer B, Boukhali M, Haas W, et al. (2015). A comprehensive Xist interactome reveals cohesin repulsion and an RNA-directed chromosome conformation. Science 349.

Mistry P, Nakabo S, O'Neil L, Goel RR, Jiang K, Carmona-Rivera C, Gupta S, Chan DW, Carlucci PM, Wang X, et al. (2019). Transcriptomic, epigenetic, and functional analyses implicate neutrophil diversity in the pathogenesis of systemic lupus erythematosus. Proc. Natl. Acad. Sci. U. S. A. 116, 25222–25228. [PubMed: 31754025]

Moindrot B., Cerase A., Coker H., Masui O., Grijzenhout A., Pintacuda G., Schermelleh L., Nesterova TB., and Brockdorff N. (2015). A Pooled shRNA Screen Identifies Rbm15, Spen, and Wtap as Factors Required for Xist RNA-Mediated Silencing. Cell Rep. 12, 562–572. [PubMed: 26190105]

Monfort A, Di Minin G, Postlmayr A, Freimann R, Arieti F, Thore S, and Wutz A (2015). Identification of Spen as a Crucial Factor for Xist Function through Forward Genetic Screening in Haploid Embryonic Stem Cells. Cell Rep. 12, 554–561. [PubMed: 26190100]

Oliva M, Muñoz-Aguirre M, Kim-Hellmuth S, Wucher V, Gewirtz ADH, Cotter DJ, Parsana P, Kasela S, Balliu B, Viñuela A, et al. (2020). The impact of sex on gene expression across human tissues. Science 369.

Pandya-Jones A, Markaki Y, Serizay J, Chitiashvilli T, Mancia W, Damianov A, Chronis C, Papp B, Chen C-K, McKee R, et al. (2020). An Xist-dependent protein assembly mediates Xist localization and gene silencing. BioRxiv 2020.03.09.979369.

Penny GD, Kay GF, Sheardown SA, Rastan S, and Brockdorff N (1996). Requirement for Xist in X chromosome inactivation. Nature 379, 131–137. [PubMed: 8538762]

Pyfrom S, Paneru B, Knoxx JJ, Cancro MP, Posso S, Buckner JH, and Anguera MC (2020). The dynamic epigenetic regulation of the inactive X chromosome in healthy human B cells is dysregulated in lupus patients. BioRxiv 2020.11.25.399022.

Quinlan AR, and Hall IM (2010). BEDTools: a flexible suite of utilities for comparing genomic features. Bioinforma. Oxf. Engl. 26, 841–842.

Reich M, Liefeld T, Gould J, Lerner J, Tamayo P, and Mesirov JP (2006). GenePattern 2.0. Nat. Genet. 38, 500–501. [PubMed: 16642009]

Rubin AJ, Parker KR, Satpathy AT, Qi Y, Wu B, Ong AJ, Mumbach MR, Ji AL, Kim DS, Cho SW, et al. (2019). Coupled Single-Cell CRISPR Screening and Epigenomic Profiling Reveals Causal Gene Regulatory Networks. Cell 176, 361–376.e17. [PubMed: 30580963]

Rubtsov AV, Rubtsova K, Fischer A, Meehan RT, Gillis JZ, Kappler JW, and Marrack P (2011). Toll-like receptor 7 (TLR7)–driven accumulation of a novel CD11c+ B-cell population is important for the development of autoimmunity. Blood 118, 1305–1315. [PubMed: 21543762]

Rubtsova K, Rubtsov AV, Cancro MP, and Marrack P (2015). Age-Associated B Cells: A T-bet–Dependent Effector with Roles in Protective and Pathogenic Immunity. J. Immunol. 195, 1933–1937. [PubMed: 26297793]

Schultz DC, Friedman JR, and Rauscher FJ (2001). Targeting histone deacetylase complexes via KRAB-zinc finger proteins: the PHD and bromodomains of KAP-1 form a cooperative unit that recruits a novel isoform of the Mi-2alpha subunit of NuRD. Genes Dev. 15, 428–443. [PubMed: 11230151]

Schultz DC, Ayyanathan K, Negorev D, Maul GG, and Rauscher FJ (2002). SETDB1: a novel KAP-1-associated histone H3, lysine 9-specific methyltransferase that contributes to HP1-mediated silencing of euchromatic genes by KRAB zinc-finger proteins. Genes Dev. 16, 919–932. [PubMed: 11959841]

Skene PJ, and Henikoff S (2017). An efficient targeted nuclease strategy for high-resolution mapping of DNA binding sites. ELife 6, e21856. [PubMed: 28079019]

Souyris M, Cenac C, Azar P, Daviaud D, Canivet A, Grunenwald S, Pienkowski C, Chaumeil J, Mejía JE, and Guéry J-C (2018). TLR7 escapes X chromosome inactivation in immune cells. Sci. Immunol. 3.

Subramanian S., Tus K., Li Q-Z., Wang A., Tian X-H., Zhou J., Liang C., Bartov G., McDaniel LD., Zhou XJ., et al. . (2006). A Tlr7 translocation accelerates systemic autoimmunity in murine lupus. Proc. Natl. Acad. Sci. U. S. A. 103, 9970–9975. [PubMed: 16777955]

Sundaram V, Cheng Y, Ma Z, Li D, Xing X, Edge P, Snyder MP, and Wang T (2014). Widespread contribution of transposable elements to the innovation of gene regulatory networks. Genome Res. 24, 1963–1976. [PubMed: 25319995]

Sunwoo H, Colognori D, Froberg JE, Jeon Y, and Lee JT (2017). Repeat E anchors Xist RNA to the inactive X chromosomal compartment through CDKN1A-interacting protein (CIZ1). Proc. Natl. Acad. Sci. U. S. A. 114, 10654–10659. [PubMed: 28923964]

Syrett CM, Paneru B, Sandoval-Heglund D, Wang J, Banerjee S, Sindhava V, Behrens EM, Atchison M, and Anguera MC (2019). Altered X-chromosome inactivation in T cells may promote sex-biased autoimmune diseases. JCI Insight 4.

Takahashi T, Ellingson MK, Wong P, Israelow B, Lucas C, Klein J, Silva J, Mao T, Oh JE, Tokuyama M, et al. (2020). Sex differences in immune responses that underlie COVID-19 disease outcomes. Nature.

Tokuyama M, Kong Y, Song E, Jayewickreme T, Kang I, and Iwasaki A (2018). ERVmap analysis reveals genome-wide transcription of human endogenous retroviruses. Proc. Natl. Acad. Sci. U. S. A. 115, 12565–12572. [PubMed: 30455304]

Tukiainen T, Villani A-C, Yen A, Rivas MA, Marshall JL, Satija R, Aguirre M, Gauthier L, Fleharty M, Kirby A, et al. (2017). Landscape of X chromosome inactivation across human tissues. Nature 550, 244–248. [PubMed: 29022598]

Wang J, Syrett CM, Kramer MC, Basu A, Atchison ML, and Anguera MC (2016). Unusual maintenance of X chromosome inactivation predisposes female lymphocytes for increased expression from the inactive X. Proc. Natl. Acad. Sci. U. S. A. 113, E2029–2038. [PubMed: 27001848]

Williamson EJ, Walker AJ, Bhaskaran K, Bacon S, Bates C, Morton CE, Curtis HJ, Mehrkar A, Evans D, Inglesby P, et al. (2020). Factors associated with COVID-19-related death using OpenSAFELY. Nature 584, 430–436. [PubMed: 32640463]

Wolf FA, Angerer P, and Theis FJ (2018). SCANPY: large-scale single-cell gene expression data analysis. Genome Biol. 19, 15.

Woodruff MC, Ramonell RP, Nguyen DC, Cashman KS, Saini AS, Haddad NS, Ley AM, Kyu S, Howell JC, Ozturk T, et al. (2020). Extrafollicular B cell responses correlate with neutralizing antibodies and morbidity in COVID-19. Nat. Immunol. 21, 1506–1516. [PubMed: 33028979]

Yang L, Kirby JE, Sunwoo H, and Lee JT (2016). Female mice lacking Xist RNA show partial dosage compensation and survive to term. Genes Dev. 30, 1747–1760. [PubMed: 27542829]

Yang L, Yildirim E, Kirby JE, Press W, and Lee JT (2020). Widespread organ tolerance to Xist loss and X reactivation except under chronic stress in the gut. Proc. Natl. Acad. Sci. 117, 4262–4272. [PubMed: 32041873]

Yao C., Bora SA., Parimon T., Zaman T., Friedman OA., Palatinus JA., Surapaneni NS., Matusov YP., Cerro Chiang G., Kassar AG., et al. . (2021). Cell-Type-Specific Immune Dysregulation in Severely Ill COVID-19 Patients. Cell Rep. 34, 108590.

Yildirim E, Kirby JE, Brown DE, Mercier FE, Sadreyev RI, Scadden DT, and Lee JT (2013). Xist RNA is a potent suppressor of hematologic cancer in mice. Cell 152, 727–742. [PubMed: 23415223]

Yuen KC, Liu L-F, Gupta V, Madireddi S, Keerthivasan S, Li C, Rishipathak D, Williams P, Kadel EE, Koeppen H, et al. (2020). High systemic and tumor-associated IL-8 correlates with reduced clinical benefit of PD-L1 blockade. Nat. Med. 26, 693–698. [PubMed: 32405063]

Zhang B, Zhang Y, Xiong L, Li Y, Zhang Y, Zhao J, Jiang H, Li C, Liu Y, Liu X, et al. (2020). CD127 imprints functional heterogeneity to diversify monocyte responses in human inflammatory diseases. BioRxiv 2020.11.10.376277.

Zhang F, Wei K, Slowikowski K, Fonseka CY, Rao DA, Kelly S, Goodman SM, Tabechian D, Hughes LB, Salomon-Escoto K, et al. (2019). Defining inflammatory cell states in rheumatoid arthritis joint synovial tissues by integrating single-cell transcriptomics and mass cytometry. Nat. Immunol. 20, 928–942. [PubMed: 31061532]

Zhang Y, Liu T, Meyer CA, Eeckhoute J, Johnson DS, Bernstein BE, Nusbaum C, Myers RM, Brown M, Li W, et al. (2008). Model-based analysis of ChIP-Seq (MACS). Genome Biol. 9, R137. [PubMed: 18798982]

Zhao R, Chen X, Ma W, Zhang J, Guo J, Zhong X, Yao J, Sun J, Rubinfien J, Zhou X, et al. (2020). A GPR174-CCL21 module imparts sexual dimorphism to humoral immunity. Nature 577, 416–420. [PubMed: 31875850]

Zumaquero E, Stone SL, Scharer CD, Jenks SA, Nellore A, Mousseau B, Rosal-Vela A, Botta D, Bradley JE, Wojciechowski W, et al. (2019). IFNγ induces epigenetic programming of human T-bethi B cells and promotes TLR7/8 and IL-21 induced differentiation. ELife 8, e41641.

Żylicz JJ, Bousard A, Žumer K, Dossin F, Mohammad E, da Rocha ST, Schwalb B, Syx L, Dingli F, Loew D, et al. (2019). The Implication of Early Chromatin Changes in X Chromosome Inactivation. Cell 176, 182–197.e23.

HIGHLIGHTS

- XIST prevents escape of genes with DNA hypomethylated promoters in B cells
- XIST maintains X-inactivation through continuous deacetylation of H3K27ac
- XIST ChIRP-MS and CRISPRi screen reveal a B cell-specific XIST cofactor TRIM28
- XIST loss and TLR7 stimulation promotes CD11c+ atypical B cell formation

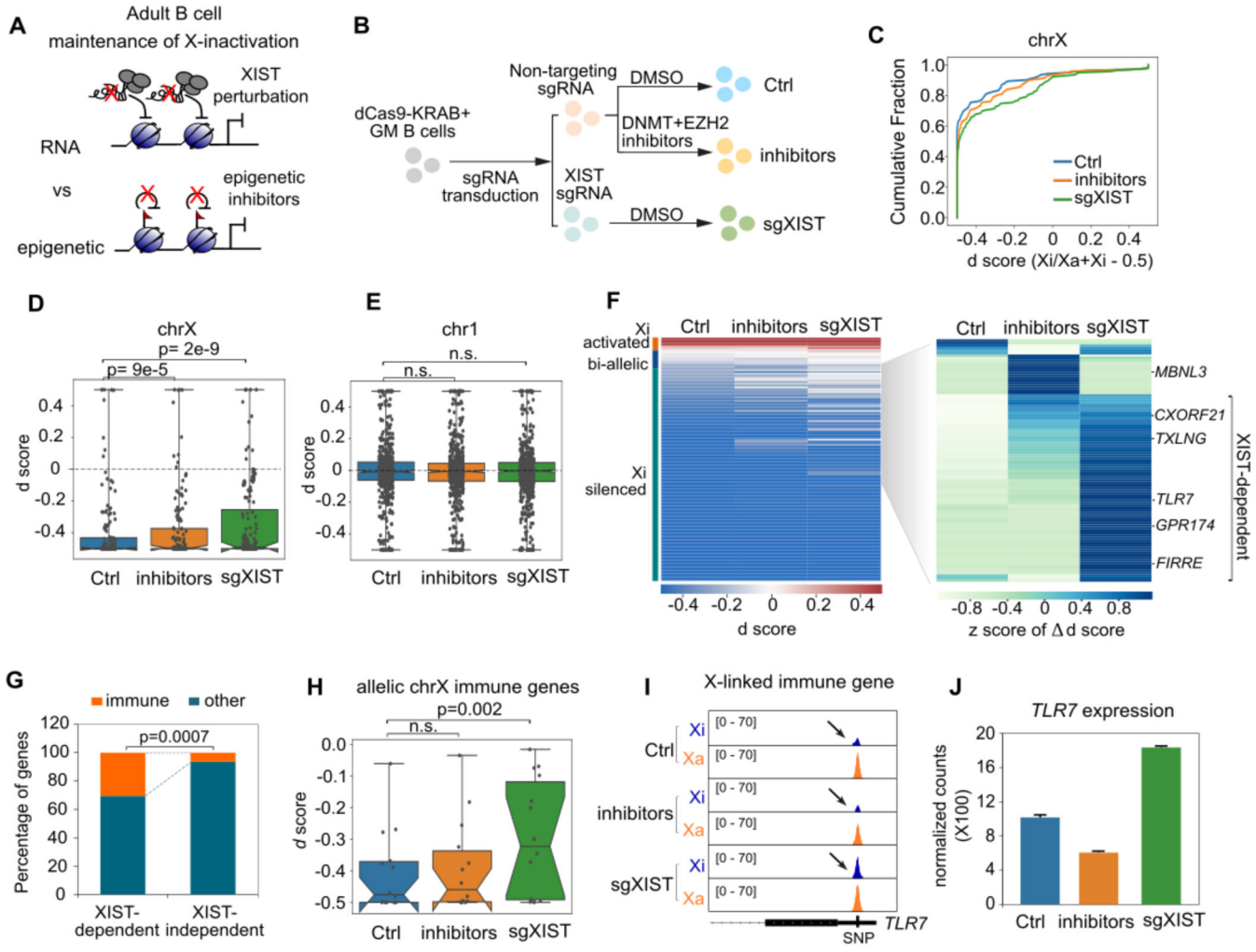

Figure 1. XIST is essential for XCI maintenance of a subset of X-linked genes.

A. Schematic view of hypothesis.

B. Schematic view of experimental set up. Control group: B cells perturbed with non-targeting control sgRNA and treated with DMSO for 7 days. Inhibitors group: B cells perturbed with control sgRNA and treated with DNA methylation and Ezh2 inhibitors for 7 days. sgXIST group: B cells perturbed with XIST sgRNA and treated with DMSO for 7 days.

C. Cumulative distribution of d-score of allelic gene expression across the X chromosome in ctrl, inhibitors and sgXIST group. P value was calculated using Kolmogorov–Smirnov test.

D and E. Box plot showing the distribution of d-score of allelic gene expression on chrX (D) and chr1 (E) between control, inhibitors and sgXIST group. P values were from paired t-test.

F. Left heatmap showing the d-score of allelic gene expression on chrX. Right heatmap showing the hierarchical clustering of genes with differential allelic expression between groups. Value depicts the z score of the difference of d-score. Representative genes are highlighted.

G. Bar plot showing the percentage of immune-related gene and genes with other functions between XIST-dependent and -independent genes. P value was from Fisher exact test.

H. Box plot showing the d-score of allelic gene expression on X-linked immune genes. P values were from paired t-test.

I. RNA-seq tracks showing the allelic expression of X-linked immune gene *TLR7*. Xa, active X chromosome. Xi, inactive X chromosome.

J. Bar plot showing the RNA-seq normalized counts of *TLR7* expression. Data are represented as mean +/− SEM

See also Figure S1 and Table S1

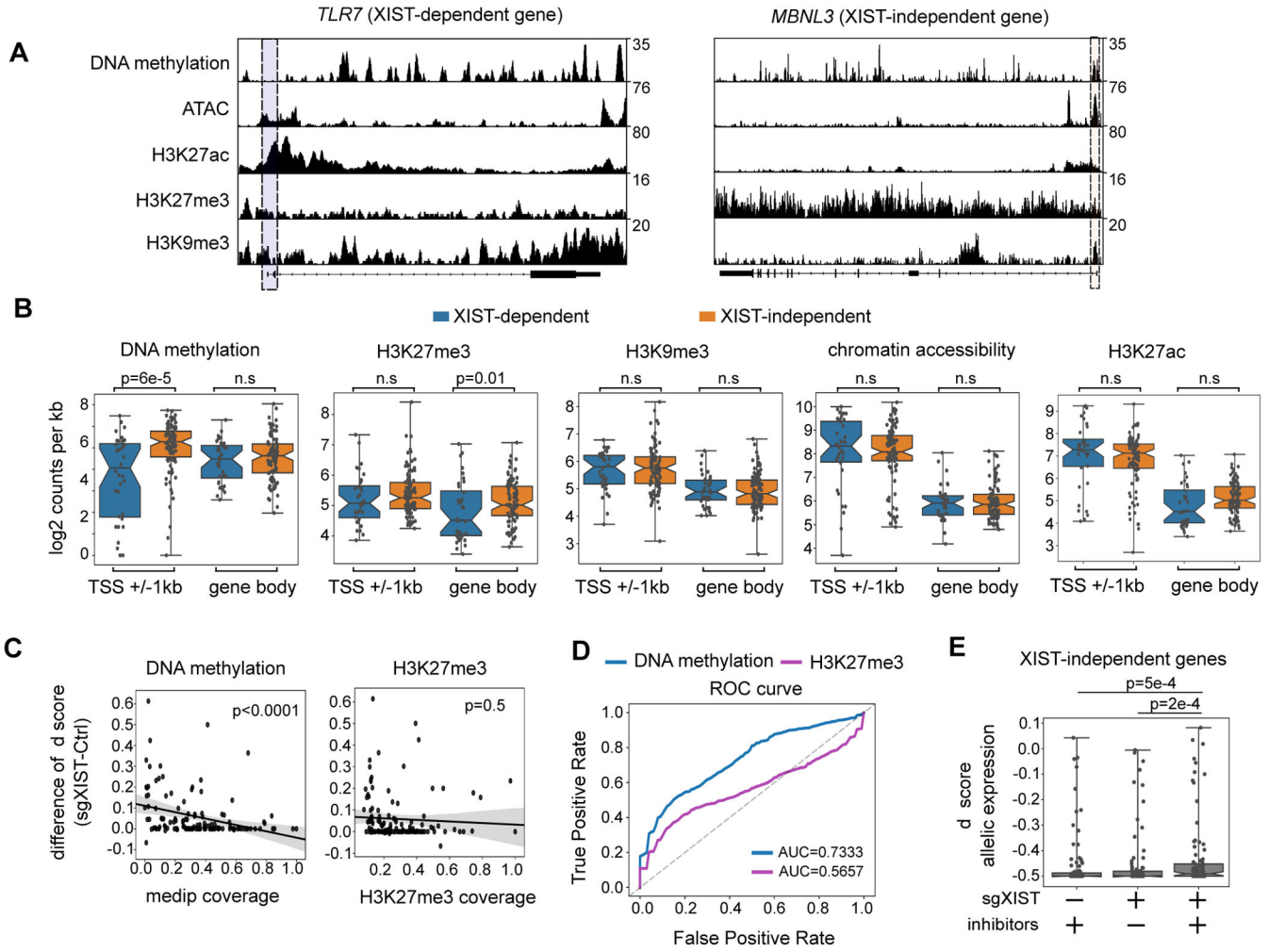

Figure 2. Low DNA methylation is associated with genes that continuously rely on Xist for XCI maintenance.

A. Genome tracks showing ATAC-seq, medip-seq, ChIP-seq of H3K27ac, H3K27me3 and H3K9me3 profiles of representative XIST-dependent (*TLR7*) and -independent (*MBNL3*) genes. Shaded area highlights the promoter regions.

B. Comparison of DNA methylation, H3K27ac, H3K27me3, chromatin accessibility and H3K9me3 between XIST-dependent and -independent genes. P value was from Mann-Whitney test.

C. Scatter plots showing the linear regression analysis of relationship between XIST dependence ($dscore^{sgXIST}$-$dscore^{ctrl}$) and epigenetic features.

D. ROC curve of logistic regression analysis showing the prediction of XIST dependence using epigenetic features DNA methylation and H3K27me3.

E. Box plot showing the d-score of XIST-independent genes between inhibitors, sgXIST, and the combination of inhibitors treatment and XIST perturbation group. P values were from paired t-test.

See also Figure S2 and Table S2

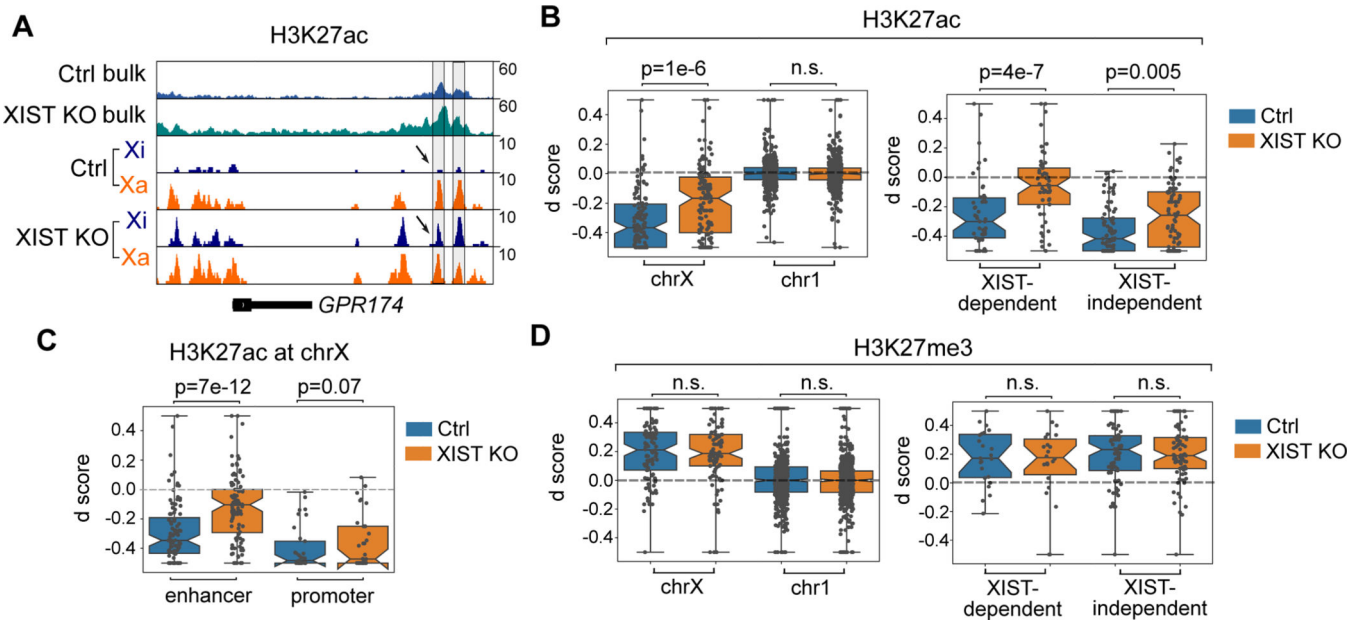

Figure 3. XIST mediates deacetylation of H3K27ac during XCI maintenance in somatic B cell line.

A. H3K27ac ChIP-seq tracks of XIST-dependent gene *GPR174*.

B. Box plots showing the d-score of chrX and chr1 genes (left), or XIST-dependent and -independent genes (right) between H3K27ac allelic profiles of control and XIST KO group.

C. Box plot showing the H3K27ac allelic bias at enhancer and promoter regions of chrX genes.

D. ox plots showing the d-score of chrX and chr1 genes (left), or XIST-dependent and -independent genes (right) between H3K27me3 allelic profiles of control and XIST KO group.

All P values were from paired t-test.

See also Figure S3

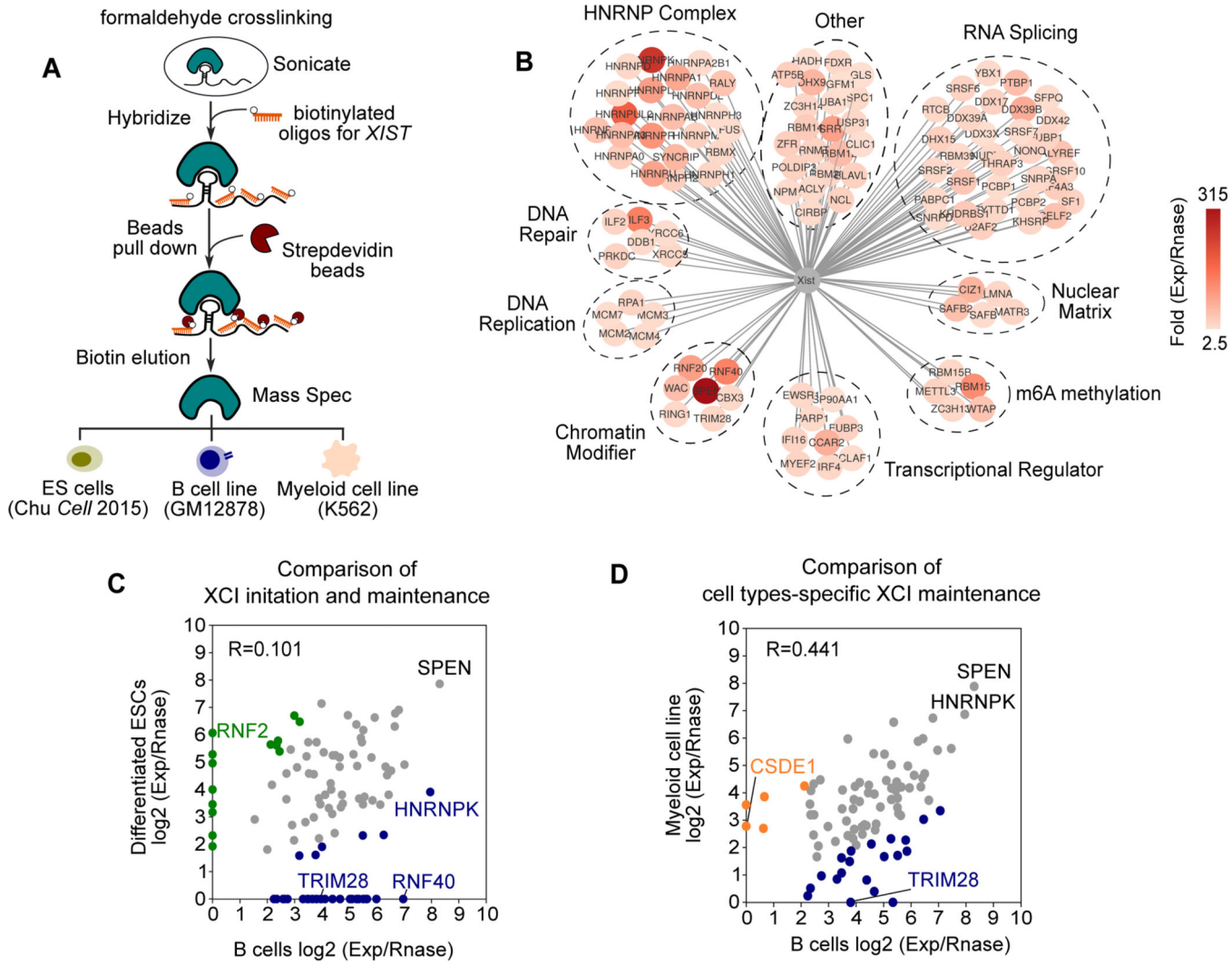

Figure 4. Identification of a unique XIST RNP complex in somatic B cell line by XIST CHIRP-MS.

A. Schematic view of ChIRP-MS of XIST bound proteins in ES cell line, GM12878 B cell line, and K562 myeloid cell line.

B. XIST RNA-associated protein network in B cell line revealed by Cytoscape. Proteins with known functions are annotated together. Color and value depicts the fold change of peptide counts of experimental group compared to Rnase treated group.

C-D. Scatter plots showing the comparison of XIST-bound protein enrichment between differentiated ES cell line and B cell line (C) or between myeloid cell line and B cell line (D). Blue: B cell-enriched proteins; green: ES enriched proteins; Orange: myeloid enriched proteins.

See also Figure S4 and Table S3

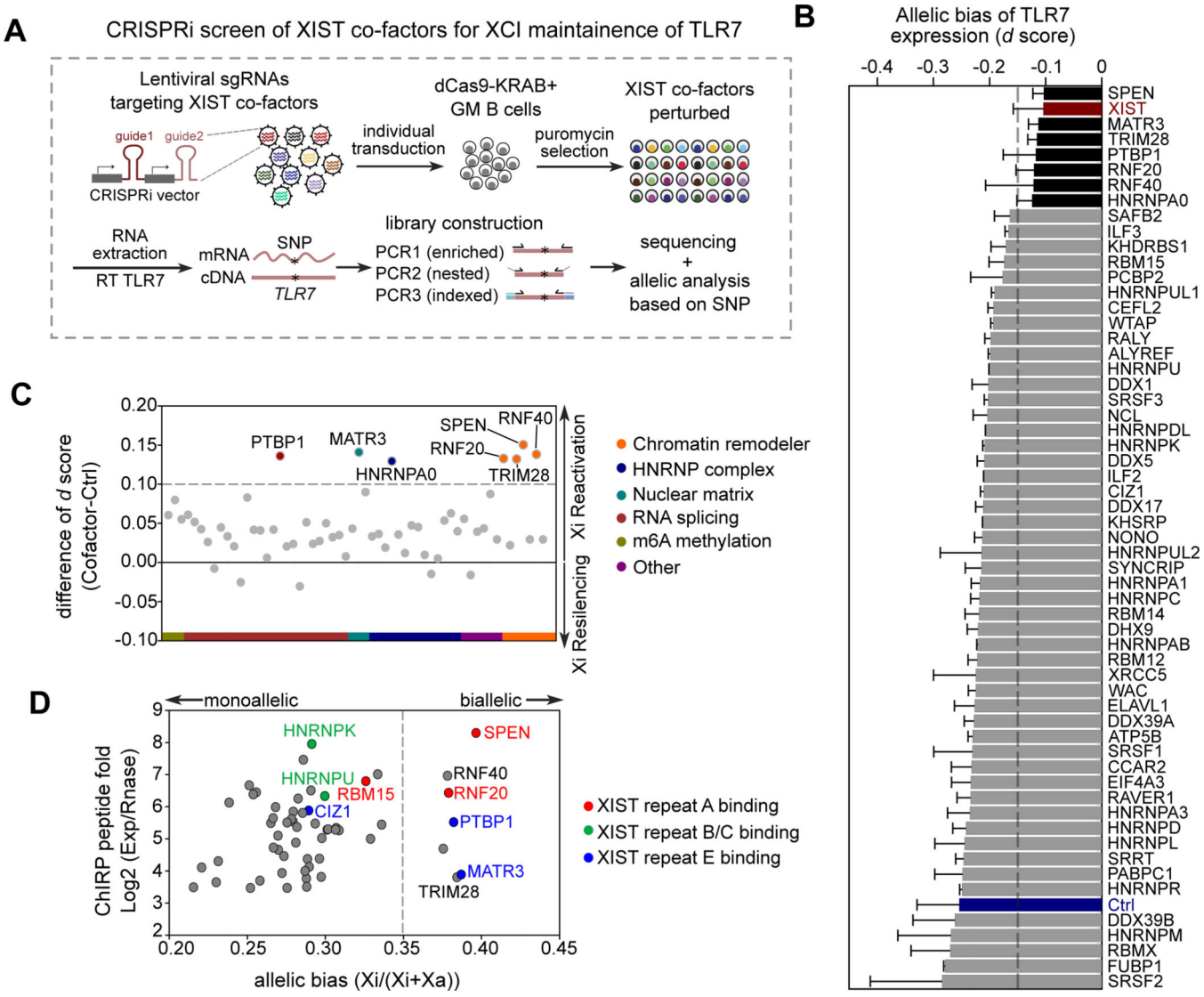

Figure 5. Allelic CRISPRi screen reveals key XIST cofactors responsible for XCI maintenance of X-linked immune gene *TLR7*.

A. Schematic view of CRISPRi screen of XIST cofactors on *TLR7* allelic gene expression.

B. Bar plot showing the mean d-score of TLR7 from two replicate screens after individual perturbation of XIST cofactors. Blue: negative control (Ctrl); red: positive control (sgXIST). Data are represented as mean +/− SEM.

C. Same as in B. The enriched co-factors compared to negative control are grouped in different functions with color labeled.

D. Scatter plot showing the co-factors with their XIST binding signal shown by fold change of peptide counts and their effect on *TLR7* allelic gene expression shown by allelic bias score. Known XIST repeat A, B/C and E binding factors are highlighted.

Gray dashed line in B-D indicates cut-off of the difference of d-score: $d\text{-score}^{\text{co-factor}}$_$\text{dscore}^{\text{ctrl}}$=0.1

See also Figure S5 and Table S4

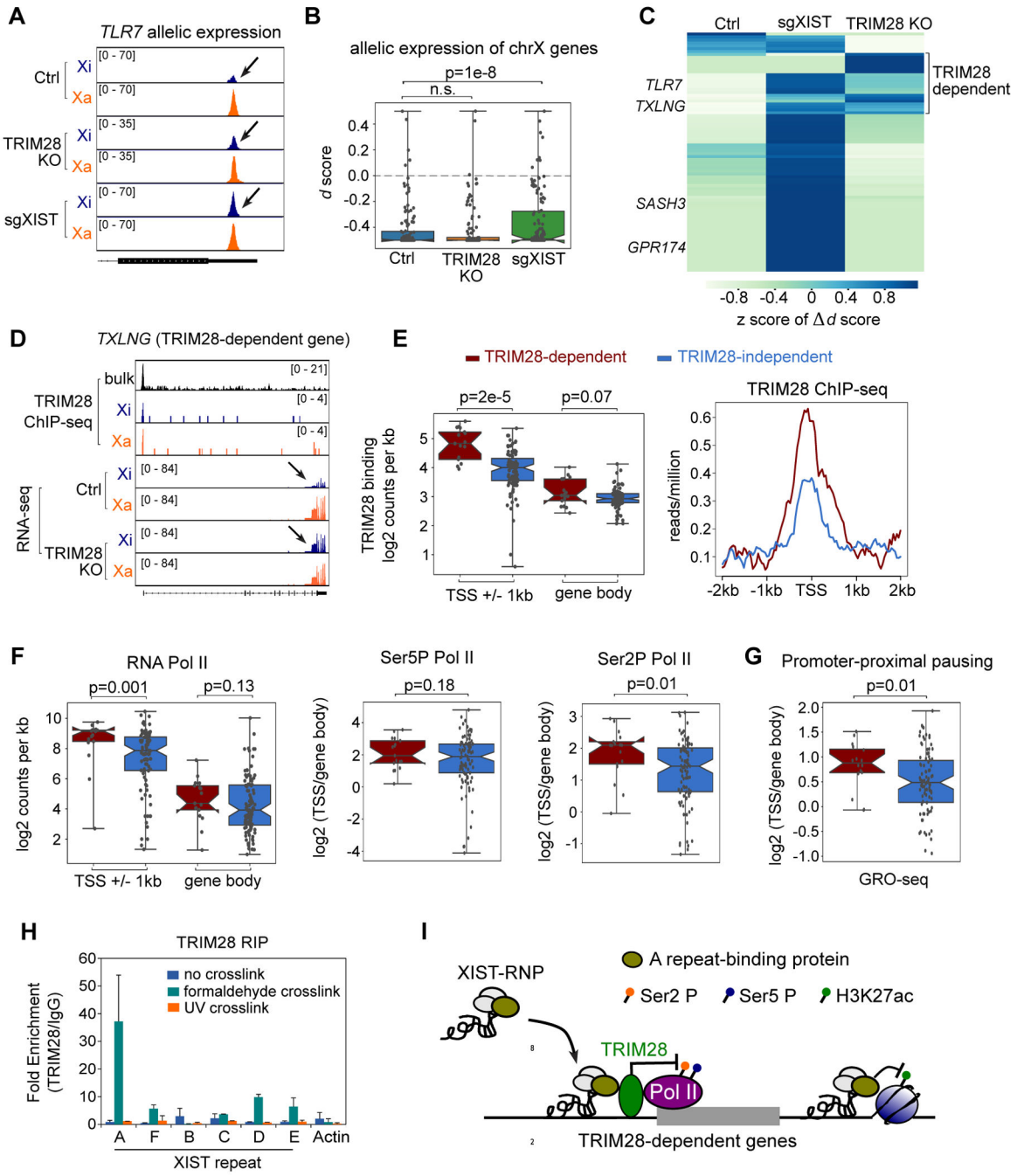

Figure 6. XIST cofactor TRIM28 participates in XCI maintenance of a subset of genes.

A. RNA-seq tracks of *TLR7* gene at Xi (blue) and Xa (yellow) between control, TRIM28 KO and sgXIST group.

B. Box plot showing the d-score of chrX genes between control, TRIM28 KO and sgXIST group. P value was from paired t-test.

C. Heatmap showing the hierarchical clustering of genes with differential allelic expression between groups. Value depicts the z score of difference of the d-score.

D. Genome tracks showing TRIM28 ChIP-seq and RNA-seq in control and TRIM28 KO cells for TRIM28-dependent gene *TXLNG.*

E. Box plot showing TRIM28 binding density at TSS+/−1kb or gene body regions between TRIM28-dependent and -independent genes (left). Average diagram showing the reads per million for TRIM28 ChIP-seq at TRIM28-dependent (red) and -independent genes (blue) at TSS +/−2kb (right).

F. Box plots showing RNA Pol II binding density (log2 counts per kb) (left), promoter pausing ratio (log2(read density^{TSS}/read density$^{gene\ body}$)) of Ser5 phosphorylated RNA Pol II (middle); and Ser2 phosphorylated RNA Pol II (right) at TRIM28-dependent (red) and -independent genes (blue).

G. Box plot showing GRO-seq analysis of Pol II promoter pausing ratio (log2(read density^{TSS}/read density$^{gene\ body}$)) at TRIM28-dependent (red) and -independent genes (blue).

H. Bar plot showing the TRIM28 RIP-qPCR on A-F repeats regions of XIST and Actin with no crosslink (blue), formaldehyde crosslink (green), and UV crosslink (orange).

I. A proposed model showing TRIM28-mediated XCI maintenance.

P values in E-G were from Mann-Whitney test.

See also Figure S6

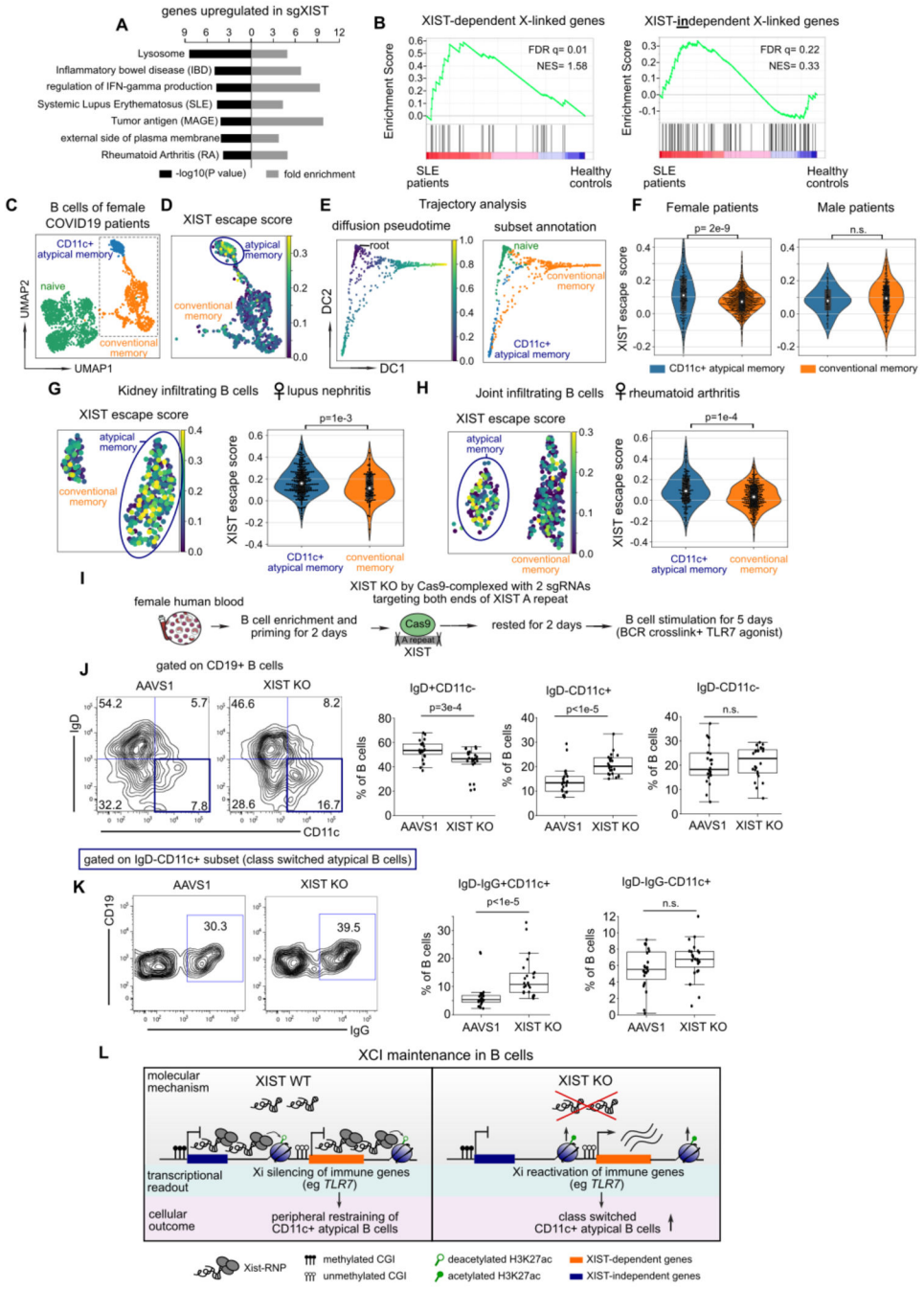

Figure 7. Escape of XIST-dependent genes in CD11c+ atypical B cells, which are increased after the loss of XIST.

A. Bar plot showing significantly enriched biological pathway and diseases from genes that are upregulated after XIST perturbation in B cell line.

B. GSEA analysis showing enrichment of XIST-dependent and -independent X-linked genes in PBMC of female SLE patients compared to healthy donors. Normalized Enrichment Score (NES) and FDR q value are shown.

C-D. Uniform manifold approximation and projection (UMAP) plot showing B cell subsets from female COVID-19 patients (C), and XIST escape score (D).

E. Diffusion map showing the pseudotime trajectory using naive cells as root (left). B cell subset projected on diffusion map (right).
F. Violin plot showing the distribution of XIST escape score between CD11c+ atypical memory B cells and conventional memory B cells in female (left) and male (right) COVID-19 patients. P value was from unpaired t-test.
G-H. UMAP showing XIST escape score of CD11c+ atypical memory cells and conventional memory B cells in kidney of female lupus patients (G), and in joint tissue of female RA patients (H). Violin plot showing the distribution of XIST escape score in two B cell subsets (right). P value was from unpaired t-test.
I. Schematic view of XIST KO in human primary B cells upon B cell activation by BCR crosslinking and TLR7 ligand stimulation.
J. Flow cytometry analysis of viable CD19+ human primary B cells between AAVS1 control and XIST KO group(left). Box plot showing the frequency of IgD+CD11c-, IgD-CD11c+, IgDCD11c-B cells among total B cells in two to three replicates from 8 female donors.
K. Flow cytometry analysis of IgG+ B cells gated on IgD-CD11c+ B cell subset. Box plot showing the frequency of IgD-IgG+CD11c+ and IgD-IgG-CD11c+ B cells among total B cells. P value in J-K was from paired t-test.
L. A proposed model of XCI maintenance in human B cells.
See also Figure S7 and Table S7

KEY RESOURCES TABLE

REAGENT or	SOURCE	IDENTIFIER
Antibodies		
Rabbit polyclonal anti-KAP1 (TRIM28)	Abcam	Cat# ab10483, RRID:AB_297222
Mouse monoclonal anti-H3K27me3	Abcam	Cat# ab6002, RRID:AB_305237
Rabbit polyclonal anti-H3K9me3	Abcam	Cat# ab8898, RRID:AB_306848
Rabbit polyclonal anti-H3K27ac	Abcam	Cat# ab4729, RRID:AB_2118291
Brilliant Violet 605™ anti-human CD27 Antibody	BioLegend	Cat# 302829, RRID:AB_11204431
Brilliant Violet 785™ anti-human IgD Antibody	BioLegend	Cat# 348241, RRID:AB_2629808
APC/Cyanine7 anti-human CD19 Antibody	BioLegend	Cat# 302217, RRID:AB_314247
PE anti-human CD11c Antibody	BioLegend	Cat# 337205, RRID:AB_1236439
PE-Cy™7 Mouse Anti-Human IgG	BD Biosciences	Cat# 561298, RRID:AB_10611712
AffiniPure $F(ab')^2$ Fragment Goat Anti-Human IgM	Jackson ImmunoResear ch Labs	Cat# 109–006-129, RRID:AB_2337553
Bacterial and Virus Strains		
10-beta Competent E.coli (High Efficiency)	NEB	Cat# C3019I
Biological Samples		
Human blood buffy coat	Stanford Blood Center	https://stanfordbloodcenter.org/research-labs/research-products-and-services/blood-products/
Chemicals, Peptices, and Recombinant Proteins		
CellXVivo Human B cell expanser	R&D Systems	Cat# CDK005
Recombinant Human IL-10	PeproTech	Cat# 200-10-2ug
Recombinant Human IL-15	PeproTech	Cat# 200-15-2ug
Recombinant Human IL-2	PeproTech	Cat# 200-02-10ug
R848	Invivogen	Cat# tlrl-r848
5-azacytidine	Sigma-Aldrich	Cat# A2385-250MG
EPZ-6438	Xcessbio	Cat# M60122-2
Critical Commercial Assays		
Direct-zol RNA Miniprep Kit	Zymo Research	Cat# R2050
NucleoSpin Gel and PCR Clean-up kit	Macherey-Nagel	Cat# 740609.250
ChIP DNA Clean & Concentrator kit	Zymo Research	Cat# D5205
Direct-zol-96 RNA Kit	Zymo Research	Cat# R2054
ZR-96 DNA Clean & Concentrator-5 (Deep Well)	Zymo Research	Cat# D4024
Direct-zol DNA/RNA Miniprep Kit	Zymo Research	Cat# R2080

REAGENT or	SOURCE	IDENTIFIER
Quick-DNA Miniprep Kit	Zymo Research	Cat# D3025
EasySep Human B Cell Enrichment Kit	stemcell technologies	Cat# 19554
KAPA Library Quantification Kit	Kapa Biosystems	Cat# KK4854
TruSeq® Stranded mRNA Library Prep Kit	Illumina	Cat#20020594
NEBNext Ultra II DNA library prep kit for Illumina	NEB	Cat#E7645S
NEBuilder® HiFi DNA Assembly Master Mix	NEB	Cat# E2621L
Deposited Data		
Raw and analyzed sequencing data	This paper	GEO GSE164596, Table S1
Raw and processed mass spectrometry data	This paper	PRIDE PXD023516, Table S3
Experimental Mocels: Cell Lines		
HEK293T	ATCC	Cat#CRL-3216
GM12878 dCas9-KRAB-BFP-2A-Blast	This paper	N/A
IMR90 dCas9-KRAB-BFP-2A-Blast	This paper	N/A
K562 dCas9-KRAB-BFP-2A-Blast	This paper	N/A
differentiated mESC	This paper	N/A
Oligonucleotides		
sgRNA sequences	This paper	Table S5
Primers for qPCR, genotyping, pyrosequencing, and CRISPRi screen	This paper	Table S6
Recombinant DNA		
pMJ117	Addgene	Cat#85997
pMJ179	Addgene	Cat#85996
pU6-sgGFP-NT1	Addgene	Cat#46914
Fuw-AcrIIA4-P2A-GFP	Addgene	Cat#108247
Flag-Trim28	Addgene	Cat#124960
Lenti-Trim28_full length	This paper	N/A
Lenti-Trim28 deltaRI NG	This paper	N/A
Lenti-Trim28 deltaPB	This paper	N/A
Software and Algorithms		

REAGENT or	SOURCE	IDENTIFIER
Bowtie2	(Langmead and Salzberg, 2012)	http://bowtie-bio.sourceforge.net/bowtie2/index.shtml
STAR	(Dobin and Gingeras, 2015)	https://github.com/alexdobin/STAR
Samtools	(Li et al., 2009)	http://www.htslib.org/
BEDTools	(Quinlan and Hall, 2010)	https://bedtools.readthedocs.io/en/latest/
SNPsplit	(Krueger and Andrews, 2016)	https://www.bioinformatics.babraham.ac.uk/projects/SNPsplit/
Htseq-count	(Anders et al., 2015)	https://htseq.readthedocs.io/en/release_0.111/count.html
MACS2	(Zhang et al., 2008)	https://github.com/macs3-project/MACS
DESeq2	(Love et al., 2014)	http://bioconductor.org/packages/release/bioc/html/DESeq2.html
Genepattern GSEA module	(Reich et al., 2006)	https://cloud.genepattern.org/gp/pages/login.jsf
Scanpy	(Wolf et al., 2018)	https://scanpy.readthedocs.io/en/stable/
Homer	(Heinz et al., 2010)	http://homer.ucsd.edu/homer/ngs/
FlowJo	TreeStar	https://www.flowjo.com/
ICE	Synthego	https://ice.synthego.com/#/